



OPEN

TiO₂-doped borate glass and glass-ceramic: properties and prospects for biological and electrical applications

Gehad Y. Abo El-Reesh¹✉, M. A. Azooz², M. A. Ouis², Amira A. Gamal³, Reham M. M. Morsi⁴, S. M. Abbas¹ & S. Abd Elkhalek¹

This study explores the synthesis, characterization, and potential applications of TiO₂-doped borate glasses and their glass-ceramics, focusing on their biological and electrical properties. Examining the impact of varying the TiO₂ content on the structural, electrical, and antimicrobial properties of the prepared samples was done. X-ray diffraction, Fourier-transform infrared spectroscopy (FTIR), density, and Field emission scanning electron microscope (FESEM) were employed to analyze the material's structural integrity and phase transitions. The AC conductivity (σ_{ac}) was measured within the frequency range of 0.042 kHz–1 MHz and at the temperature range of 298–573 (K). The estimated DC conductivity proved that incorporating of TiO₂ at the expense of BaO results in higher conductivity values than those of the free glass and glass ceramic samples. The prepared samples exhibited a semiconducting nature. The dielectric constant (ϵ') values increase upon doping with TiO₂. The incorporation of TiO₂ improved the bioactivity (antimicrobial) of the studied glasses, making it suitable for biomedical applications such as drug delivery and tissue engineering. Also, the long-term stability and cytotoxicity were evaluated. The results indicate that TiO₂-doped borate glasses and glass-ceramics present a promising avenue for the development of multifunctional materials that meet the demands of both biological and electrical applications.

Keywords Borate glass, Glass-ceramic, TiO₂, Antimicrobial, Electrical properties

Borate glass is considered as a wide glass former that has the ability to alter its properties depending on the type and quantity of the additives that may be incorporated into the glass composition^{1,2}. B₂O₃ can exist as triangular [BO₃] and tetrahedral [BO₄] structural units in the glass matrix due to the ability of boron to alter its coordination number with oxygen^{3,4}. Borate-based glass can be included in various applications such as radioactive waste immobilization, ionic conductors, smart windows manufacturing, plant nutrition agri-glass, high power solid state laser, and bioactive materials^{5–11}. Glass can be used as a bioactive material through its use as bone fillers, toothpaste and composites, dental cement, treating burns and wounds, synthetic scaffolds and bioactive antibacterial materials^{12–15}. Borate glass materials exhibit a higher level of bioactivity than silicates and this is attributed to their lower chemical durability, higher rate of hydroxyapatite (HA) conversion, and fast rate of dissolution in biological fluids^{16,17}. They have also been exhibited to enhance wound healing, cell proliferation, and cell differentiation^{18,19}. Borate glasses exhibit antibacterial effects and inhibition of several species of Gram-positive and Gram-negative bacteria^{20,21}. Replacing SiO₂ in the commercial glass system S53P4 with B₂O₃ with (25, 50, 75, and 100 mol%) shows improved antibacterial effects against E.coli bacteria compared to the base system²². Glass-ceramics can be obtained through the crystallization of glasses by thermal heat treatment. Bioactive glass-ceramics have been evaluated for their biological effects. As reported^{23–25}, controlled crystallization of glass samples decreases their reaction kinetics with physiological solution ions without the inhibition of HA precipitation, even in the case of intensively crystallized glass-ceramics. Da Silva et al. evaluated the effect of crystallization (as a function of heat treatment time) of the prepared glass ceramics on their bioactive and antibacterial properties²¹. The bacterial infections that arise from surgical procedure failure or nosocomial

¹Chemistry Department, Faculty of Science, Beni-Suef University, Beni-Suef, Egypt. ²Glass Research Department, National Research Centre, Dokki, Giza, Egypt. ³Chemistry of Natural and Microbial Products Department, Pharmaceutical and Drug Industries Research Institute, National Research Centre, Dokki, Cairo, Egypt. ⁴Physical Chemistry Department, National Research Centre, 33 El Bohoth St., Dokki, P.O. 12622, Giza, Egypt. ✉email: gehad_yahia@science.bsu.edu.eg; gehad_yahia93@yahoo.com

infections lead to bone implant failures during the treatment of bone fractures using glass. The activity of antibacterial glass can be enhanced through doping antibiotics²⁶ or trace amounts of ions that can cause antibacterial effects that can be slowly released, e.g. silver (Ag^+), copper (Cu^{2+}), zinc (Zn^{2+}), strontium (Sr^{2+}) and titanium (Ti^{2+})^{27–30}. Titanium is considered a 3d transition metal that can be added to the glass matrix to modify glass properties like electrical, thermal, structural, and optical properties^{31–33}. In glass networks, titanium can present in both trivalent and tetra-valent oxidation states depending on the glass composition, the condition of melt, and its concentration^{34,35}. In borate glass, titanium ions exist as a network former (TiO_4 or $\text{B}-\text{O}-\text{Ti}$) and glass modifier (TiO_6) groups³⁶. The presence of a small amount of TiO_2 in glass can improve glass's chemical durability, forming the ability of glass to act as a nucleating agent during heat treatment^{37–39}. Depending on the porosity of bioactive glass^{40,41} and the ability to adjust its reaction rate by altering its composition⁴², incorporated ions (TiO_2) leach out of glass in a controlled delivery release over an extended range of time⁴³. Titanium has been known to have its antibacterial effects and has also been included in different materials to inhibit the growth of bacteria^{44–46}. Samudrala et al.⁴⁷ produced a borosilicate glass composition doped with TiO_2 to improve biological response in bone tissue engineering fields, and they observed antibacterial activity of 2% TiO_2 in the system against *S. aureus* and *E. coli*. The electrical properties of glass-ceramics are significantly influenced by their composition and the controlled crystallization process. For instance, the material's dielectric behavior in the $\text{BaO}-\text{Al}_2\text{O}_3-\text{SiO}_2-\text{B}_2\text{O}_3$ system was affected by varying the amounts of B_2O_3 , BaO , and crystallization temperatures⁴⁸. Borate glasses doped with titanium dioxide (TiO_2) in the system $20\text{Na}_2\text{O}-(20-x)\text{CdO}-60\text{B}_2\text{O}_3-x\text{TiO}_2$ ($0 \leq x \leq 5$ mol%), have garnered significant interest due to their distinctive electrical properties⁴⁹. Further investigations into borate glasses within the $\text{B}_2\text{O}_3-\text{Na}_2\text{O}-\text{TiO}_2$ system have examined the effects of varying TiO_2 concentrations on both optical and electrical properties. Dielectric measurements reveal that the dielectric constant (ϵ') is influenced by the TiO_2 content. Additionally, the direct current (DC) conductivity of these glasses is found to be temperature-dependent, with higher TiO_2 concentrations leading to increased conductivity. These findings suggest that TiO_2 acts as a modifier in the glass network, affecting the mobility of charge carriers and thus the electrical properties⁵⁰. Enhancing the electrical and thermal expansion coefficient of borosilicate glasses doped with TiO_2 and its counterpart glass ceramics was investigated⁵¹. Borate glass is generally insulating in nature; the addition of transition metal oxides (TMO), such as V_2O_5 , Fe_2O_3 , CuO , WO_3 , TiO_2 , and MoO_3 , to the glass, makes it an electronic conducting semiconductor⁵². The semiconducting properties of this type of glass are due to the ability of TMO to present more than one valence state⁵². Structural, electrical, thermal expansion coefficient (TEC), and hardness were studied to examine the impact of including transition metal ions on enhancing the electrical and TEC of borosilicate glasses doped with TiO_2 and its counterpart glass ceramics. The prepared glass-ceramic was found to be suitable for use in electronics and solar cell applications based on its overall thermal and electrical properties⁵¹. The purposes of this study are: (1) Preparation of TiO_2 -modified glass samples by substitution of BaO in the glass system ($40\text{B}_2\text{O}_3-20\text{Al}_2\text{O}_3-10\text{NaF}-(30-X)\text{BaO}-X\text{TiO}_2$) mol % and their corresponding glass ceramics; (2) Characterization of the prepared samples by various tools including Fourier transform infrared spectroscopy (FT-IR), X-ray diffraction (XRD), Field emission scanning electron microscopy (FESEM), Density and Molar volume; (3) Studying the effect of gradual increasing of TiO_2 mol% on structural, electrical and biological properties; (4) Electrical properties and dielectric behavior of these samples have been characterized, which may be suitable for use in electronic devices; (5) Evaluating the bioactivity of the materials to determine their suitability for biomedical applications, including antimicrobial activity.

Experimental section

Materials

All raw materials were used directly without previous purification. Orthoboric acid (H_3BO_3 , Winlab, Leicestershire, UK, Assay 99.5%) for B_2O_3 , anhydrous heavy barium carbonate (BaCO_3 , E. Merck, Darmstadt, Germany) for BaO , Titanium dioxide (Fluka, Germany) for TiO_2 , Aluminium oxide (Fluka, chemei AG, switzer land) and Sodium fluoride.

Synthesis of materials

Glass synthesis

In this study, a traditional melt annealing method was employed for the preparation of the glass system ($\text{B}_2\text{O}_3-\text{Al}_2\text{O}_3-\text{NaF}-\text{BaO}-\text{TiO}_2$) where a series of four TiO_2 -modified glass compositions were prepared by replacing BaO in the glass composition with TiO_2 . The glass batch was weighed accurately and put into a platinum crucible. The melt was synthesized in an electric furnace at 1375 °C for 2 h. The melts were continuously rotated at time intervals to maintain the homogeneity of melts and get rid of bubbles. Stainless steel molds were pre-heated to cast the melt and then transferred at once into a muffle furnace optimized at 400 °C for annealing for 1 h, then left to cool to room temperature. The symbol of the base glass is BG0, whereas the symbols of the four modified glasses are BG1, BG2, BG3, and BG4, respectively. Table 1 represents the glass composition in mol%.

Glass-ceramic synthesis

The glass-ceramic materials were synthesized through thermal heat treatment of the parent prepared glass samples. First, the glass samples were heated to the temperature of nucleation (480 °C) at a rate of 5 °C/min for 4 h. Then, the temperature was elevated to the crystal growth temperature (750 °C) at a rate of 5 °C/min, and the samples were kept at this temperature for 6 h. The samples were left to cool at a rate of 25 °C/min to room temperature. The symbol of the base glass-ceramic is BGC0 where, the symbols of the four modified glass-ceramics are BGC1, BGC2, BGC3, and BGC4, respectively.

Glass code	B ₂ O ₃	Al ₂ O ₃	NaF	BaO	TiO ₂
BG0	40	20	10	30	–
BG1	40	20	10	29.5	0.5
BG2	40	20	10	29	1
BG3	40	20	10	28.5	1.5
BG4	40	20	10	28	2

Table 1. Composition of base glass and the series of TiO₂ modified glass in mol%.

X-ray diffraction analysis

X-ray diffraction (XRD) patterns were obtained for glass-ceramic samples with a PANalytical (Empyrean) X-ray diffraction using Cu K α radiation (wave length 0.154 cm⁻¹) at an accelerating voltage of 40 KV, current of 35 mA, scan angle range from 20° to 70° and scan step 0:02°.

FTIR spectral measurements

The Fourier transform infrared (FT-IR) spectra (4000–400 cm⁻¹) were obtained by a Bruker (Vertex 70) spectrometer for both glass and glass-ceramic samples using the KBr technique. The powder samples were mixed with pulverized KBr at a ratio of 1:100 mg. The mixtures were pressured at 5 tons/cm² to produce homogenized discs. Immediately, the prepared discs were measured.

Density measurements

Density was done through the standard Archimedes method at room temperature, with distilled water as an immersion liquid. Three samples of each glass were employed to calculate the density. The values are precise to ± 0.02 g/cm³. Density can be calculated by using the Eq. (1)

$$\rho = W_a \rho_w / (W_a - W_w) \quad (1)$$

Where ρ is the density of the glass sample, W_a and W_w are the weights of the glass sample in both air and distilled water, respectively, and ρ_w is the density of distilled water.

The molar volume, which is known as the volume of one-gram mole of glass, can be calculated by the relation (2).

$$V_m = 1/\rho \sum X_i M_i \quad (2)$$

Where, $X_i M_i$ are the components of molar fraction and molecular weight.

Field emission scanning Electron microscope (FESEM) images

The morphology of the glass-ceramic samples was examined by SEM type (JEOL- JSM- T2O Japan) after coating them with surface layers of gold.

Electrical measurements

The AC conductivity (σ_{ac}) of the prepared samples was measured using the LRC Hi-Tester (HIOKI, 3532-50), Japan, over a frequency range from 0.042 kHz to 1 MHz and a temperature range from 298 to 573 (K). Increasing the temperature was provided by increasing the input voltage of a variac transformer connected to a wire-wound resistance heater. The temperature was determined using a copper/Constantine thermocouple in proximity to the sample. The AC conductivity, σ_{ac} , is calculated using the relation (3).

$$\sigma_{ac} = \omega \epsilon_0 \epsilon' \tan \delta \quad (3)$$

Where ω is the angular frequency, ϵ_0 is the permittivity of free space, equals 8.85×10^{-12} F m⁻¹, and ϵ' is the dielectric constant which is determined from expression (4).

$$\epsilon' = Cd/\epsilon_0 A \quad (4)$$

Where d represents the thickness of the sample, and A represents the sample surface area. The capacitance, C , and the dissipation factor, $\tan \delta$, are obtained directly from the instrument for the studied samples⁵³.

Biological activities experiments

Microbial strains

Five microorganisms were selected for testing the antimicrobial activity. Two G+ve strains (*Staphylococcus aureus*, *Bacillus cereus*), one G-ve bacteria strain (*Escherichia coli*), one yeast (*Candida albicans*), and one fungus (*Aspergillus niger*) were obtained as clinical strains from El-Demerdash hospital, Cairo, Egypt.

Inoculum preparation

All used media were sterilized for inoculum preparation; nutrient broth medium was used for bacteria while potato dextrose broth medium was used for fungus and yeast. The tubes were incubated for 24 h at 37 °C for bacteria and 2–3 days at 30 °C for yeast and fungi.

Determination of antimicrobial assay

The ten samples (glass) were in vitro evaluated for their antimicrobial activity. Standard and clinically isolated microorganism strains were used for antimicrobial assays such as *E. coli* (Gram-negative bacteria), *Bacillus cereus* (Gram-positive bacteria), *Staphylococcus aureus* (Gram-positive bacteria), *Candida albicans* (yeast), and *Aspergillus niger* (fungi) by measuring the growth inhibition of pathogenic organisms according to⁵⁴. Samples (0.03 g) were added to the tubes [10 mL of nutrient broth (bacteria and yeast) or potato dextrose broth (fungi)]. The inoculated tubes (100 µl from the inoculum) and standard tubes (without adding samples) were incubated for 24 h at their optimum growth temperatures (37 °C for bacteria and 28 °C for yeast and fungi), and the optical densities (O.D) of the microbial growth were measured by spectrophotometer at 600 nm. Experiments were carried out in triplicate for each strain of the evaluated microorganisms. The reported results are the average.

$$\text{N.B: Inhibition of microbial growth (\%)} = 100 - [(\text{O.D of sample (trial)}) / (\text{O.D of standard})]$$

Longer-term stability assessments

To evaluate the long-term antimicrobial stability of the glass and glass ceramic samples, the same antimicrobial assay protocol described previously was applied. However, in this case, the samples had been stored under ambient laboratory conditions for approximately one year before testing. The test was carried out against the same microbial strains using identical incubation conditions.

Cytotoxicity assay

Mammalian cell lines: HFB 4 cells (Human normal melanocytes cell line) were obtained from the American Type Culture Collection (ATCC, Rockville, MD). **Chemicals Used:** Dimethyl sulfoxide (DMSO), Fetal Bovine serum, MTT and trypan blue dye were purchased from Sigma (St. Louis, Mo., USA). DMEM, HEPES buffer solution, L-glutamine, gentamycin and 0.25% Trypsin-EDTA were purchased from Lonza (Belgium).

Cell line propagation The cells were propagated in Dulbecco's modified Eagle's medium (DMEM) supplemented with 10% heat-inactivated fetal bovine serum, 1% L-glutamine, HEPES buffer, and 50 µg/ml gentamycin. All cells were maintained at 37°C in a humidified atmosphere with 5% CO₂ and subcultured two times a week.

Cytotoxicity evaluation using viability assay For cytotoxicity assays, the cells were suspended in medium at concentration 1×10^5 cell/well in Corning® 96-well tissue culture plates, and incubated for 24 h. The tested compounds were then added into 96-well plates (three replicates) to achieve eight concentrations for each compound. Six vehicle controls with media or PBS were run for each 96-well plate as a control. After incubating for 24 h, the numbers of viable cells were determined by the MTT test. Briefly, the media was removed from the 96-well plate and replaced with 100 µl of fresh culture DMEM medium without phenol red, then 10 µl of the 12 mM MTT stock solution (5 mg of MTT in 1 mL of PBS) to each well, including the untreated controls. The 96-well plates were then incubated at 37 °C and 5% CO₂ for 4 h. An 85 µl aliquot of the media was removed from the wells, and 50 µl of DMSO was added to each well and mixed thoroughly with the pipette and incubated at 37 °C for 10 min. Then, the optical density was measured at 590 nm with the microplate reader (SunRise, TECAN, Inc, USA) to determine the number of viable cells, and the percentage of viability was calculated through Eq. 5.

$$[(\text{ODt} / \text{ODc})] \times 100\% \quad (5)$$

Where OD_t is the mean optical density of wells treated with the tested sample and OD_c is the mean optical density of untreated cells. The Cytotoxic concentration (CC₅₀), the concentration required to cause toxic effects in 50% of intact cells, was estimated from graphic plots of the dose response curve for each conc. Using Graphpad Prism software (San Diego, CA, USA).

Results and discussion**X-ray diffraction measurements**

Figure 1 Exhibits XRD patterns of three selected glass samples (BG0, BG2, and BG4) and their corresponding crystallized samples (glass-ceramics) (BGC0, BGC2, and BGC4). Figure 1a displayed broad humps arising from the amorphous nature of the prepared glass samples. As shown in Fig. 1b, certain crystalline phases were separated through heat treatment of the parent glass samples. These crystalline phases are Ba₃B₂O₆ (card no 96-156-8109), Ba₅B₄O₁₁, AlBaBO₃F₂ (card no 96-152-6215), and Al₂O₃ in addition to BaTi₂O₅ and BaTiO₃ phases related to incorporation of TiO₂ into the matrix (in BGC2 and BGC4 samples). For BGC0, broad humps with weak intensity peaks of crystalline phases were observed. Since TiO₂ acts as a nucleating agent⁵⁵, the gradual increase of TiO₂ content caused an increase in peaks intensity of the formed crystalline phases, indicating continuous growth of crystal grains in the glass matrix⁵⁶. The quantitative crystalline phases composition is displayed in Table 2.

FTIR study

Figure 2 shows the FTIR spectra over a range from 2000 to 400 cm⁻¹ of the base and doped TiO₂ borate glass samples. The figure exhibits the characteristic vibrational bands of both triangular and tetrahedral borate groups

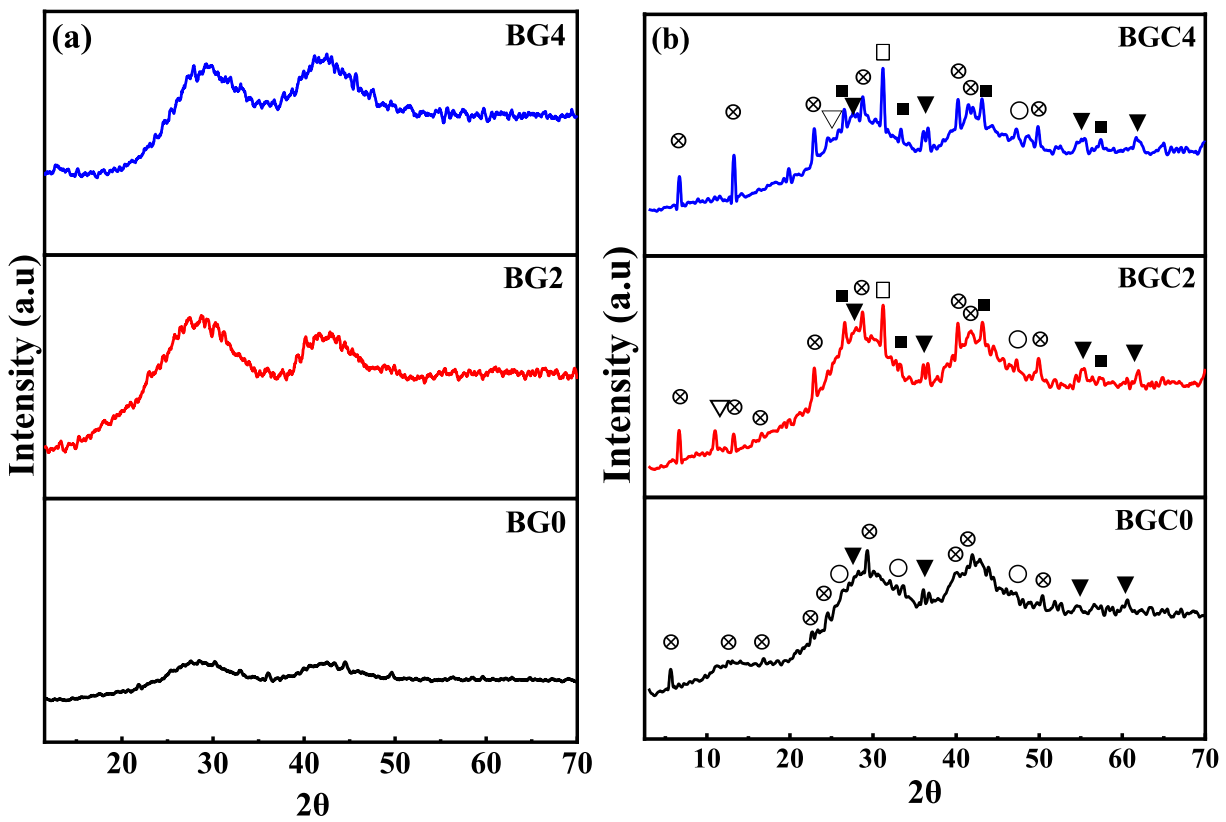


Fig. 1. XRD patterns of three selected (a) glass samples (BG0, BG2 and BG4) and (b) their corresponding glass ceramics (BGC0, BGC2 and BGC4 where, \otimes $\text{Ba}_3\text{B}_2\text{O}_6$, \square $\text{Ba}_5\text{B}_4\text{O}_{11}$, \blacktriangledown $\text{AlBaBO}_3\text{F}_2$, ∇ Al_2O_3 , \blacksquare BaTi_2O_5 , \square BaTiO_3 .

Samples code	Crystalline phases %					
	$\text{Ba}_3\text{B}_2\text{O}_6$	$\text{Ba}_5\text{B}_4\text{O}_{11}$	$\text{AlBaBO}_3\text{F}_2$	Al_2O_3	BaTi_2O_5	BaTiO_3
BGC0	54	24	32	-	-	-
BGC2	40	5	17	7	16	15
BGC4	43	6	19	-	17	15

Table 2. The quantitative crystalline phases composition.

in their specific vibrational regions. As shown in Fig. 2, the mid infrared region ($1600\text{--}400\text{ cm}^{-1}$) is the region where B-O vibrations are dominant. This region can be distinguished into three broad bands^{57–61}, which are:

- The strong vibrational band ranging from ($1120\text{--}1600\text{ cm}^{-1}$) appeared due to the stretching vibrations of triangular borate units (BO_3 and BO_2O^-).
- The absorption band from ($820\text{--}1120\text{ cm}^{-1}$) is assigned to the symmetric and asymmetric stretching of B-O in BO_4 tetrahedral group units.
- The area ranging from ($420\text{--}820\text{ cm}^{-1}$) is related to the bending vibrations of B-O-B in $[\text{BO}_3]$ and $[\text{BO}_4]$ units, B-O-Ti and TiO_4 ⁶².

Figure 3 shows the FTIR spectra of all synthesized glass samples and their spectra deconvolution. Deconvolution of the bands gives a good chance for a more precise explanation of the overlapping bands. As expected, the FTIR spectra of these glass samples have both triangular BO_3 and tetrahedral BO_4 vibrational bands and the absorption band intensities caused by tetrahedral borate groups $[\text{BO}_4]$ at ($820\text{--}1120\text{ cm}^{-1}$) are lower than that caused by triangular borate groups $[\text{BO}_3]$ at ($1120\text{--}1600\text{ cm}^{-1}$). This is attributed to the presence of alkali (NaF) and alkaline earth oxides (BaO) that can transform BO_3 group units into BO_4 units to a certain limit (16–20 mol%), after which the surplus of BaO supports the formation of non-bridging oxygen⁶³. These results were also obtained by Kamitsos in his study on alkali oxides (LiO_2 , K_2O , Na_2O) and alkaline earth oxides (BaO , SrO , CaO) in borate glass⁶⁴. The FTIR spectral curves of doped TiO_2 borate glass samples (BG1, BG2, BG3, and BG4) are noticed to be closely similar to the corresponding base sample (BG0) with the same characteristic broad bands but with some shifts to lower or higher wavenumber of some peaks caused by the addition of TiO_2 into

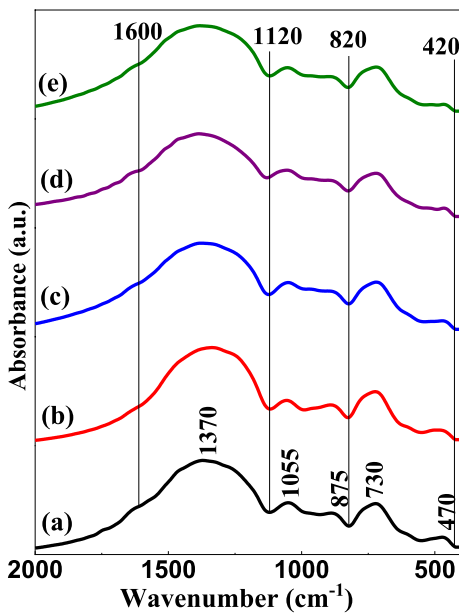


Fig. 2. FTIR absorption spectra of base and doped TiO_2 borate glass samples where, (a) BG0, (b) BG1, (c) BG2, (d) BG3, (e) BG4.

glass composition^{35,65}. As explained by Marzouk et al.⁶², the vibrational bands of crystalline TiO_2 are located within the wavenumber range from 400 to 800 cm^{-1} , which is the same region of appearance of borate groups bending vibrations, indicating that vibrations of TiO_2 doped glass at (400–800 cm^{-1}) are composite of merged bands which contain overlapping BO_3 , BO_4 , B-O-Ti, and TiO_4 vibrations. It is worth mentioning that introducing TiO_2 into glass composition creates some observed changes which can be discussed as follows^{1,62,66,67}:

- (I) The band at about 492 cm^{-1} , which is related to O-B-O and vibrations of metal cations (Ba^{2+}) shifts to a lower wavenumber at about (468–487 cm^{-1}) and this is attributed to vibrations of added Ti^{2+} .
- (II) The vibrational band located at 634 cm^{-1} , which is identified due to the in-plane bending of BO_3 units, shifts to a lower wavenumber at about (585–611 cm^{-1}), in addition to the appearance of a new band in (BG2, BG3, and BG4) at (695–699 cm^{-1}) on the gradual increasing of TiO_2 content. This band can be assigned to asymmetric (Ti-O-Ti) stretching vibrations of TiO_6 .
- (III) The vibrational absorption peak at 733 cm^{-1} , which refers to the bending vibration of the B-O-B linkage, is completely overlapped with the band of TiO_4 (B-O-Ti) bending, leading to the creation of the overlapped band at (759–767 cm^{-1}).

From the above assumptions, one can conclude that at lower concentrations of TiO_2 , TiO_4 (network former) structural units are mainly present in the network and there is a gradual increase in the formation of TiO_6 (network modifier) structural units with an increase in TiO_2 content. The assignments of the observed vibrational absorption bands are summarized in Table 3. Figure 4 shows FTIR spectra of glass-ceramic samples. The FTIR displays the same characteristic spectral bands as their parent glasses, but these vibration modes are noticed to be sharper with split peaks related to the fine crystalline derivatives of three and four co-ordinated borate groups⁶⁸.

Density measurements

Density is considered the simplest tool that can help to understand the changes occurring in the structure of the glass network. The density depends on the compactness, the geometrical configurations, the coordination number, the cross-link densities, and the dimensions of the interstitial spaces of the glass⁷⁵. The influence of the substitution of TiO_2 at the expense of BaO on the measured density and the calculated molar volume of the studied glass system is demonstrated in Fig. 5 a. As illustrated, the substitution of BaO by TiO_2 caused a slight decrease in density from 3.494 g/cm^3 to 3.273 g/cm^3 , this can be mainly attributed to the lower molecular weight of TiO_2 (79.867 g/mol) than BaO (153.33 g/mol). Glass density is directly proportional to the molecular weight of glass and inversely proportional to molar volume (related to ionic radius). Since the ionic radius of Ti^{2+} is smaller than Ba^{2+} , the overall decrease in density indicates that the molecular weight change is more effective on density than the ionic radius change⁷⁶. The molar volume of glass linearly increased from 28.173 cm^3/mol to 29.627 cm^3/mol with increasing TiO_2 in the glass matrix as shown in Fig. 5a. As expected, the density and molar volume of glass exhibited opposite behaviour. The volume expansion may be related to the gradual formation of octahedral TiO_6 structural units by increasing TiO_2 content in the glass matrix (as deduced from the FTIR study). These TiO_6 units act as a network modifier and hence increase the amount of non-bridging oxygen which produces an open structure and increase the interstitial positions in the glass network^{37,38,77}. Also, the molar

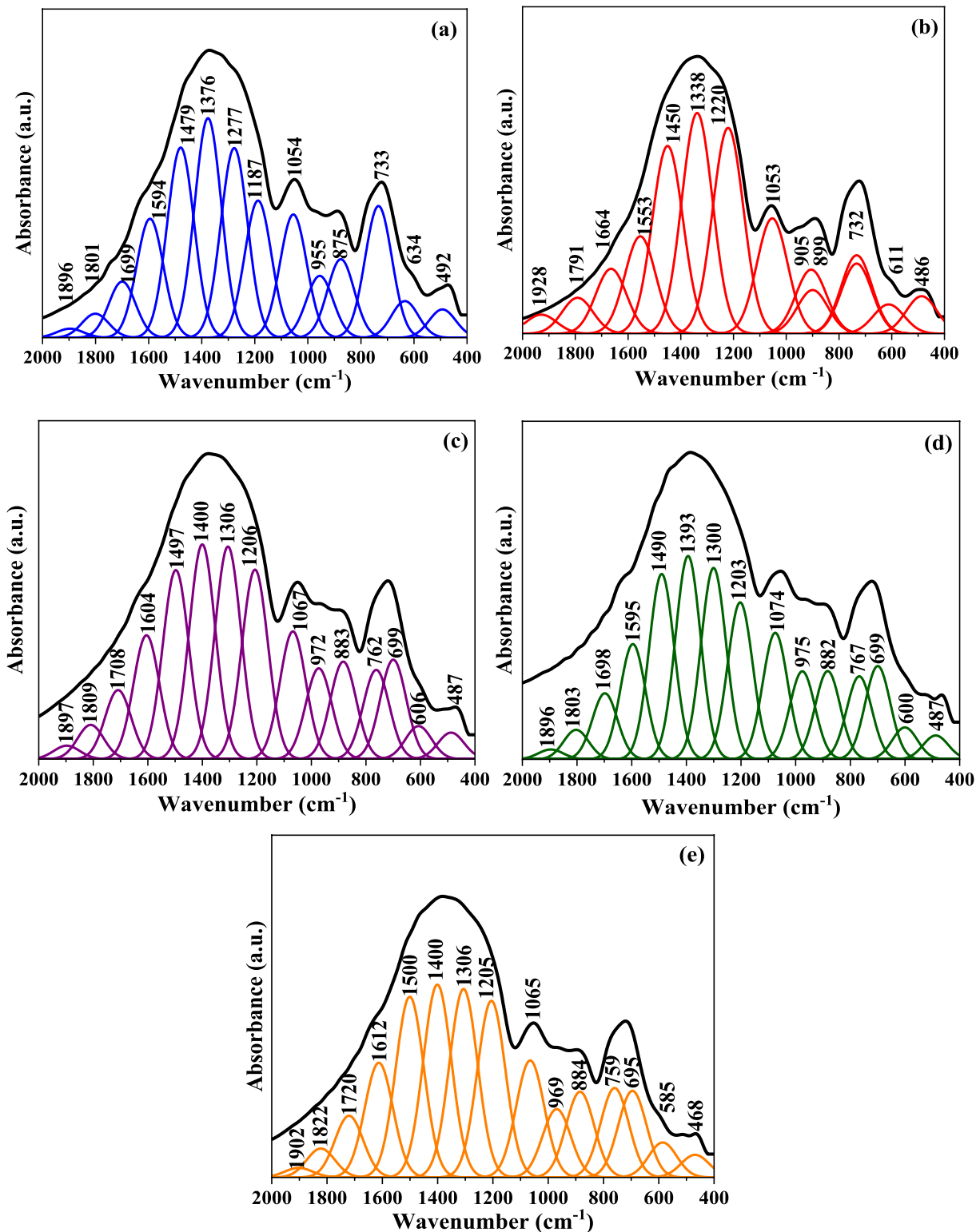


Fig. 3. Deconvoluted IR spectra of (a) BG0, (b) BG1, (c) BG2, (d) BG3, (e) BG4.

volume increase may be associated with the increase in the total number of oxygen atoms by substitution of BaO by TiO_2 , leading to the expansion of the glass network⁷⁶. As shown in Fig. 5b, the density of the synthesized glass samples is lower than that of their corresponding glass-ceramics. According to^{78,79}, heat treatment relaxes the glass structure by releasing some of its internal energy, the thing which causes rearrangement and compactness of the structure. All the values of density, molar mass, and molar volume of glass, and the density of glass ceramics are listed in Table 4.

Peak no.	Wavenumber (cm ⁻¹)					Assignments
	BG0	BG1	BG2	BG3	BG4	
1	492	486	487	487	487	Vibrations of metal cations Ba ²⁺ , Ti ²⁺
2	634	611	606	600	585	In plane bending vibrations of BO ₃ units.
3	-	-	699	699	695	asymmetric (Ti-O-Ti) stretching vibrations of TiO ₆
4	733	732	762	767	759	bending vibration of B-O-B linkage and TiO ₄ (B-O-Ti) bending
5	875	899	883	882	884	
6	955	905	972	975	969	BO ₄ stretching of tri-, penta, and diborate groups
7	1054	1053	1067	1074	1065	
8	1187	1220	1206	1203	1205	
9	1277	-	1306	1300	1306	
10	1376	1338	1400	1393	1400	Asymmetric stretching vibrations of (BO ₃ , BO ₂ O ⁻)
11	1479	1450	1497	1490	1500	
12	1594	1553	1604	1595	1612	
13	1699	1664	1708	1698	1720	
14	1801	1791	1809	1803	1822	Vibrations of water, OH groups.
15	1896	1928	1897	1896	1902	

Table 3. Assignments of the observed vibrational absorption bands^{69–74}.

Scanning electron microscope (SEM) images

Figure 6 shows the SEM micrographs of three selected BGC0, BGC2 and BGC4 glass-ceramic samples. It is obvious that the micrographs of all the selected samples exhibit a crystalline structure (as supported by XRD data) which consists of multiple layers (sheets). Unlike the base one BGC0 (without TiO₂), increasing TiO₂ content makes the layers more compacted, defined and rigid with smooth edges (layer edges without fractures).

Electrical measurements

Figure 7 illustrates the frequency dependence of the alternating-current conductivity (σ_{ac}) at different temperatures in the frequency range extending from 0.042 kHz to 1 MHz for samples BG0 and BGC0 (as representative samples). It can be observed that the conductivity σ_{ac} increases with increasing frequency. This observation suggests that the electrical conductivity of the material is a thermally activated process⁸⁰. The increase in AC conductivity of the material with increasing frequency can be attributed to the release of space charges caused by a decrease in the material's barrier properties⁸¹. The variation observed in Fig. 7 reveals that the conductivity increases strongly with frequency at lower temperatures, while the increase is lower at higher temperatures. It is generally known⁸² that AC conductivity is influenced by both the polarization of immobile ions (e.g., Al²⁺, B²⁺) within the borate network and the mobility of charge carriers. The conductivity due to charge carriers is small at low temperatures. Accordingly, the AC conductivity is expected to exhibit the observed frequency dependence (Fig. 7), which depends mainly on the polarization of immobile ions. The conductivity of the charge carriers is expected to increase with temperature⁸³. At high temperatures, the dominant factor in the conductivity will be the mobility of the charge carriers, while the polarization of the immobile ions will make a less significant contribution. Therefore, at high temperatures, the AC conductivity will have a lower dependence on frequency as shown in (Fig. 7). For example, the σ_{ac} of the sample BGC0 at 25 °C increases from 2.84×10^{-10} to 2.65×10^{-6} (S.cm⁻¹) at 1 kHz and 1 MHz, respectively, and at 300 °C increases from 1.73×10^{-6} to 6.03×10^{-5} (S.cm⁻¹) at 1 kHz and 1 MHz, respectively. The DC part is independent of frequency, is dominant at low frequencies and appears as a flat DC plateau at low-frequency regions. By extrapolating the plateau regions observed in Fig. 7, to zero frequency, the DC conductivity values of the samples can be estimated⁸⁴. The DC electrical conductivity (σ_{dc}) was plotted against the reciprocal temperature for all samples studied as shown in Fig. 9.

Figure 8a, b shows the variations in AC conductivity as a function of the reciprocal of the temperature at different frequencies for un-doped glass and glass ceramic samples (as representative samples). It is noticed that the conductivity increases with increasing temperature, which indicates that they have semiconducting properties⁸⁵. The values of the activation energies associated with AC conduction ($E_{a(ac)}$) were calculated, in the high-temperature region, from the slopes of the linear fit (Fig. 8) and listed in Table 5. These values are in the range of 0.317–0.693 (eV) and 0.172–0.446 (eV) for glass and glass ceramic samples, respectively. It is also observed from Fig. 8, and the data in Table 5, that the slopes of the curves decrease as frequency rises. Consequently, the $E_{a(ac)}$ values decrease as the applied field frequency increases, which may be attributable to electron jump-enhancement between localized states⁸⁶.

Figure 9 shows the temperature dependence of DC conductivity (σ_{dc}) of all glass samples with the composition 40B₂O₃-20Al₂O₃-10 NaF-(30-x)BaO- xTiO₂ and their corresponding glass ceramics, featuring varying TiO₂ content in the temperature range 25°–300 °C. It is found that the estimated σ_{dc} increases with increasing temperature across the entire temperature range, indicating their semiconducting nature⁸⁷. The investigated samples show a linear dependence of the logarithm of conductivity (log σ_{dc}) on the reciprocal of absolute temperature (1/T), Fig. 9. This feature reveals the thermally activated mobility of the charge carriers according to the hopping conduction mechanism⁸⁸ that can be described by the Arrhenius relation (6).

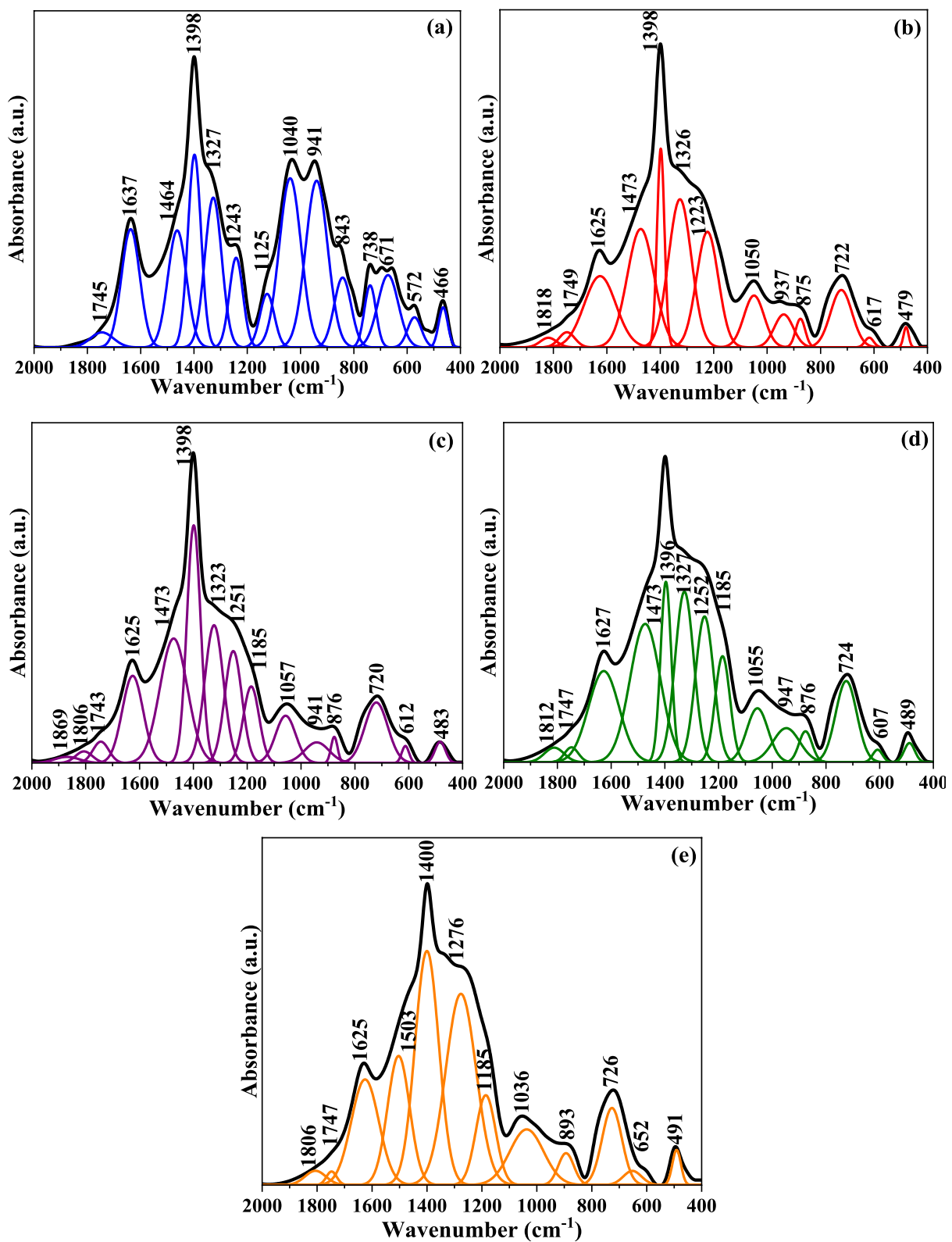


Fig. 4. Deconvoluted IR spectra of (a) BGC0, (b) BGC1, (c) BGC2, (d) BGC3, (e) BGC4.

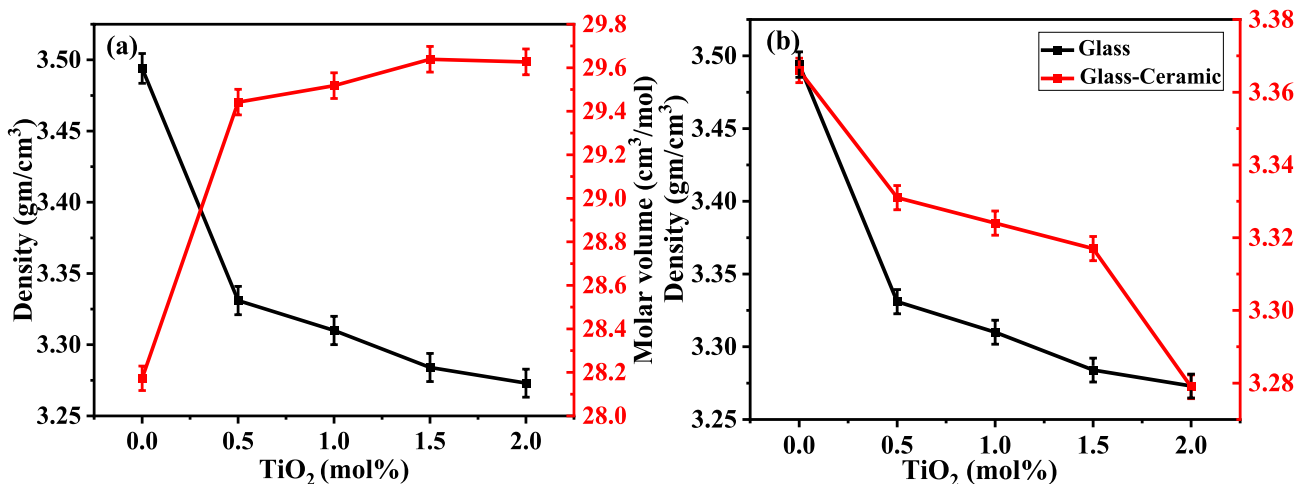


Fig. 5. Density and molar volume of glass (a) and density of glass and glass-ceramics (b).

Samples code		Density (g/cm^3)	Molar mass (g/mol)	Molar Volume (cm^3/mol)	Samples code		Density (g/cm^3)
Glass	BG0	3.494	98.438	28.173	Glass-Ceramics	BGC0	3.366
	BG1	3.331	98.0707	29.442		BGC1	3.331
	BG2	3.310	97.7034	29.518		BGC2	3.324
	BG3	3.284	97.3361	29.639		BGC3	3.317
	BG4	3.273	96.9688	29.627		BGC4	3.279

Table 4. Density and molar volume of glass and glass-ceramics.

$$\sigma_{dc} = \sigma_0 \exp(-E_a/kT) \quad (6)$$

Where σ_0 is the pre-exponential factor, E_a is the activation energy for the conduction process, k is the Boltzmann's constant and T is the absolute temperature. In the high-temperature region ranging from 130 to 300 °C, the DC activation energies ($E_{a(dc)}$) are determined from the slopes of the straight lines of the $\log \sigma_{dc}$ plots versus $1000/T$ plots and the values are listed in Table 6. The range of activation energy values falls in the range of 0.053–0.728 (eV) and 0.037–0.462 (eV) for glass and glass ceramic samples, respectively. From Fig. 9a, it can be noticed that the σ_{dc} of the sample BG0 exhibits a non-linear increase with the measuring temperature rising, featuring two distinct regions. These two regions are formed by two different mechanisms. The first region, at lower temperatures ranging from room temperature up to approximately 110 °C, is characterized by low activation energy (0.156 eV). This behavior was attributed to electronic conduction⁸⁹, which may occur via small polaron hopping between defect states, such as oxygen vacancies that can present in the structure of amorphous glass systems⁹⁰. While the second mechanism observed at higher temperatures (130–300 °C) exhibits higher activation energy. This is primarily due to the predominance of ionic movement mechanisms driven by the mobility of charge carriers, specifically Na^+ ions.

Furthermore, for doped glass samples and for all glass ceramics, it is evident that the electrical conductivity (σ_{dc}) increases linearly with rising temperature, accompanied by relatively lower activation energies than the parent glass (Table 6). This behaviour can be attributed to the electronic mechanism coming from the electronic transition between Ti^{3+} and Ti^{4+} , which may exist by introducing TiO_2 to the samples and increasing its content. These ions may participate in the increase of conductivity and decrease the activation energy values (Table 6). The transfer of these electrons could be considered as a small polaron hopping process⁹¹. In the glass ceramic samples (Fig. 9b), in addition to the above explanation, the participation of electronic conduction that lowers the $E_{a(dc)}$ values may also come from the fact that within the bulk sample, the oxygen vacancies are usually created during heat treatment due to the loss of oxygen which are usually created during sintering and brings free electrons behind, making an n-type material⁹². When the temperature is increased, the created electrons become conduction electrons due to thermal activation energy⁹³. The decrease of the $E_{a(dc)}$ by doping with TiO_2 suggests that the conduction in doped samples is mainly electronic.

Variations of both room temperature DC electrical conductivity (σ_{dc}) and activation energies ($E_{a(dc)}$) as a function of TiO_2 concentration (in mol%) are represented in Fig. 10. It is evident from this figure that the σ_{dc} increases with increasing TiO_2 content in glass as well as glass ceramics. This increase may be attributed to an increase in the number of non-bridging oxygen (NBO) and, as a result, increasing in the open structure through which the charge carriers can move with higher mobility^{94,95}. These results are in good agreement with the FTIR results, where increasing TiO_2 content at the expense of BaO , supports the formation of non-bridging oxygen.

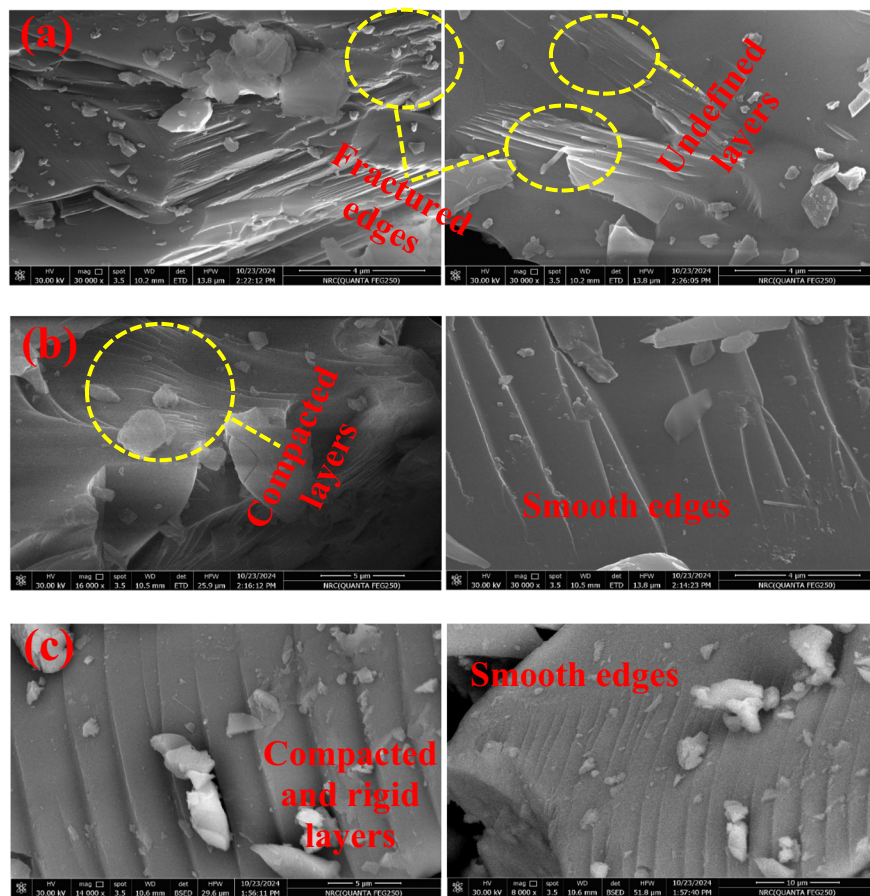


Fig. 6. SEM micrographs of three selected (a) BGC0, (b) BGC2 and (c) BGC4.

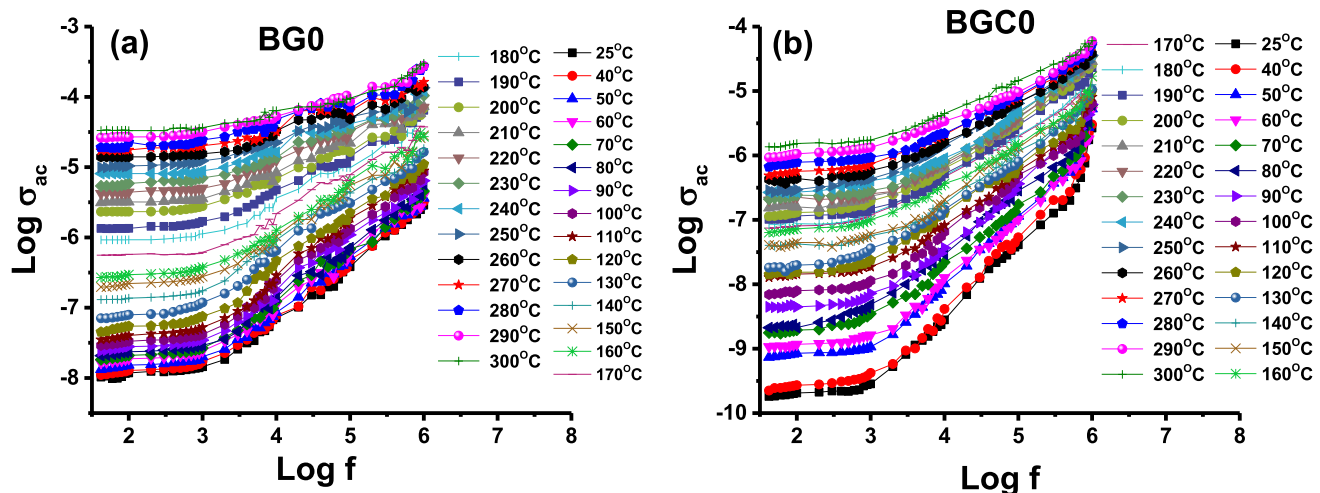


Fig. 7. Variation of $\log \sigma_{ac}$ as a function of applied frequency for samples (a) BG0 and (b) BGC0 at different temperatures.

Virender Kundu et al. reported that the formation of NBOs causes a decrease in band gap energy and, as a result, the DC conductivity increases⁹⁶. Therefore, such structural changes can have an important influence on the mobility of Na^+ , which has the same concentration in all the samples under investigation, wherein the Na^+ mobility increases in the presence of non-bridging oxygen atoms^{97,98}. Besides, the electron hopping between Ti^{4+} and Ti^{3+} ions as referred to before. These conditions may contribute to an increase in conductivity with the incorporation of TiO_2 . For example, σ_{dc} at room temperature increases from 9.82×10^{-9} to 2.86×10^{-6}

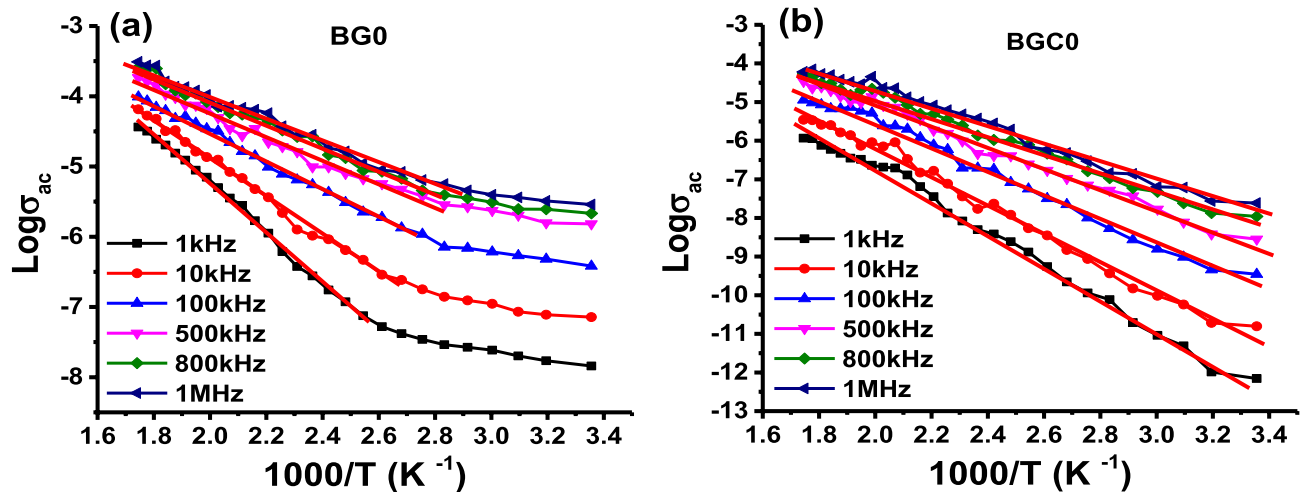


Fig. 8. Variation of AC conductivity (σ_{ac}) with reciprocal of temperature for samples (a) BG0 and (b) BGC0 at different frequencies.

Samples Code		$E_{a(ac)}$ (eV)					
		1 kHz	10 kHz	100 kHz	500 kHz	800 kHz	1 MHz
Glass	BG0	0.693	0.538	0.397	0.333	0.326	0.317
Glass ceramic	BGC0	0.446	0.374	0.300	0.283	0.220	0.172

Table 5. The AC activation energy ($E_{a(ac)}$) at different frequencies for BG0 and BGC0 samples.

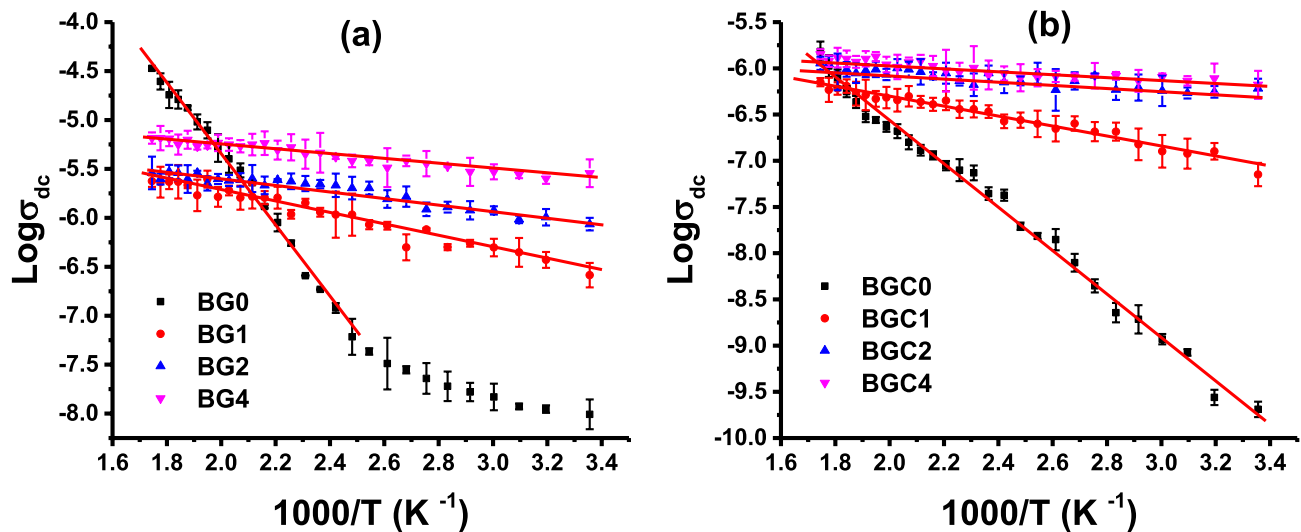


Fig. 9. Variation of DC conductivity (σ_{dc}) as a function of the reciprocal temperature for all samples (a) glasses and (b) glass ceramics at room temperature.

($\text{S} \cdot \text{cm}^{-1}$) and from 2.04×10^{-10} to 6.64×10^{-7} ($\text{S} \cdot \text{cm}^{-1}$) for glasses and glass ceramic, respectively, as the TiO_2 concentration increases from 0 to 2 mol%. Notably (Fig. 10b), in the case of glass ceramic samples, the increase in conductivity seems to be nearly constant at higher contents of TiO_2 ($x = 1.5, 2$ mol %). This behavior can be due to the compactness and rigidity of the glass ceramic structure produced by increasing TiO_2 content that confirmed by SEM. This may affect the mobility of the charge carriers and, consequently, the rate of increasing conductivity is retarded. Also, in doped samples, the values of activation energy ($E_{a(dc)}$) (Table 6) reveal the dominance of the electronic mechanism over the ionic transfer one.

Additionally, it is obvious (Table 6) that the σ_{dc} of the parent glass sample BG0 is higher than that of its glass ceramic BGC0. This can also be attributed to the rigid and dense structure caused by glass crystallization,

Samples Code	Glasses				Glass ceramics			
	BG0	BG1	BG2	BG4	BGC0	BGC1	BGC2	BGC4
$E_{a(dc)}$ (eV)	0.728	0.12	0.065	0.053	0.462	0.107	0.035	0.037
σ_{dc} (S/cm)	9.82×10^{-9}	2.60×10^{-7}	8.62×10^{-7}	2.86×10^{-6}	2.04×10^{-10}	7.10×10^{-8}	6.05×10^{-7}	6.64×10^{-7}
ϵ' , 1 kHz	42.17	204.31	304.31	393.28	94.95	308.55	454.58	477.21

Table 6. The DC activation energy ($E_{a(dc)}$), the DC conductivity (σ_{dc}) at room temperature (RT) and the dielectric constant (ϵ') at 1 kHz and at RT for all samples.

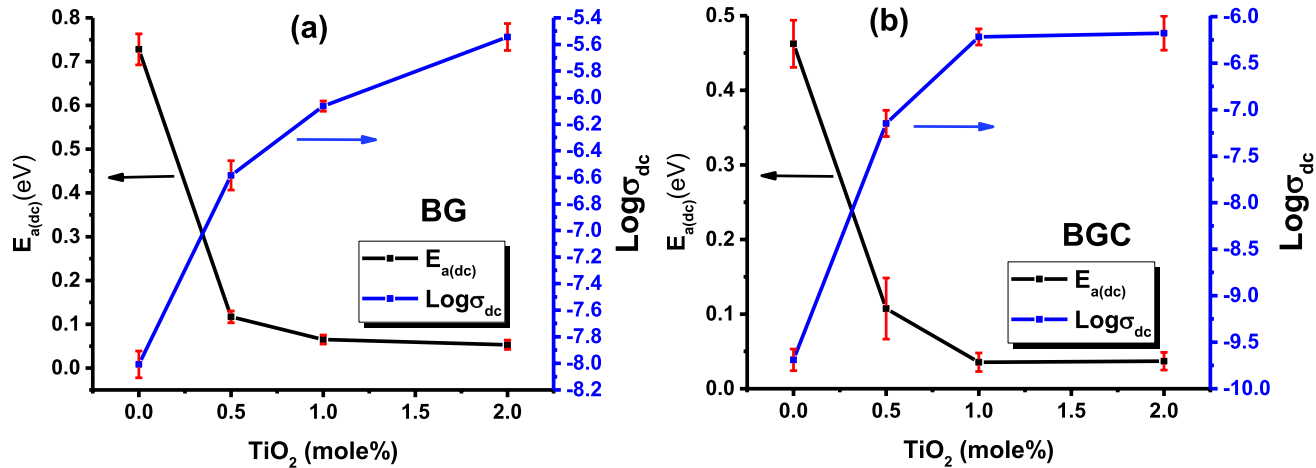


Fig. 10. The variation of the σ_{dc} at 298 K, and the activation energy ($E_{a(dc)}$) as a function of mole fractions of TiO_2 for all the investigated samples (a) glasses (b) glass ceramics.

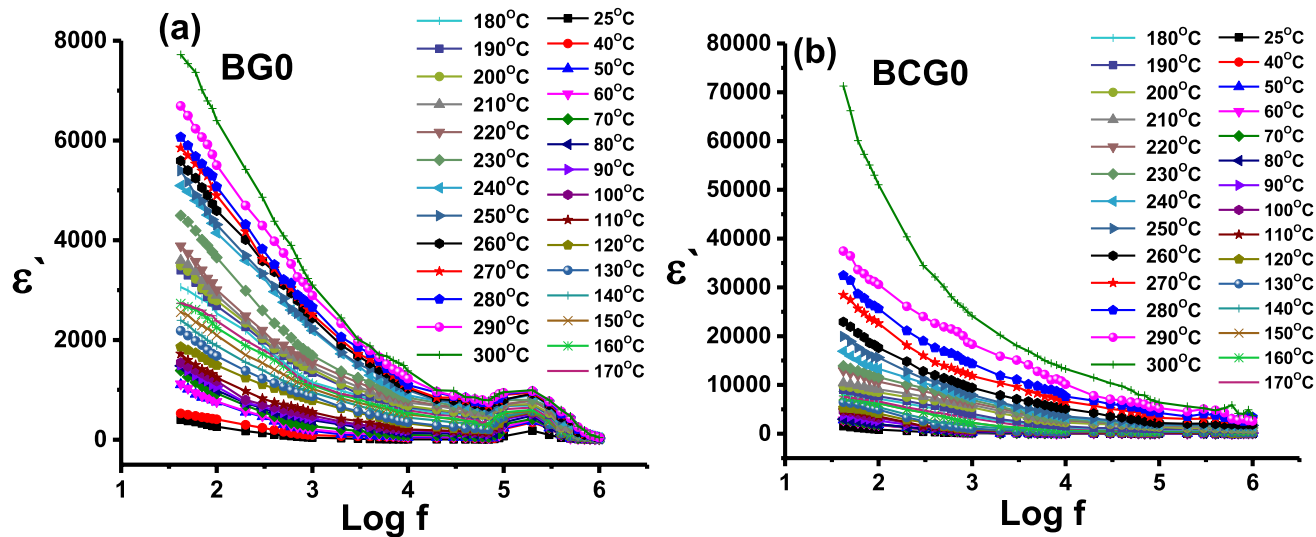


Fig. 11. Variation of dielectric constant (ϵ') versus frequency for samples (a) BG0 and (b) BCG0 at different temperatures.

which further hinders charge transport and decreases the conductivity values of glass ceramic than that of glass. This behavior follows that reported in other literature⁹⁹. Furthermore, it was reported that semiconductors have conductivity values between 10^3 and 10^{-8} S.cm⁻¹¹⁰⁰. Since the studied samples doped with TiO_2 have room temperature conductivity values in the range 10^{-8} – 10^{-6} S/cm and exhibited a semiconducting nature; therefore, the doped samples studied can be considered as semiconducting materials.

The dielectric constant values are plotted as a function of frequency for samples BG0 and BCG0 (as representative samples) at different temperatures in Fig. 11. It can be seen that the samples showed high values

of the dielectric constant at low frequency and high temperature. The higher ϵ' values at lower frequencies were attributed to the contribution of the multi-component polarizability (i.e. electronic, ionic, orientation, and space charge)¹⁰¹. Interfacial contains defects such as vacancies and vacancy clusters. Thus, the space charges can move under the application of an external field and when they are trapped by the defects, lots of dipoles (space charge polarization) are formed^{102,103}. Whereas, as the frequency increases, the dipoles are no longer able to rotate and their oscillation begins to lag behind the field, so the dielectric constant decreases and approaches nearly a constant value at high frequency¹⁰⁴.

The increase in ϵ' with temperature is predicted to occur due to the weakening of the binding force between molecules/atoms with the increase in temperature, permitting the molecules/ atoms to vibrate more and more, which in turn increases the polarization, hence an increase in the dielectric constant ϵ' ^{105,106}.

Figure 12 shows the frequency dependence of the dielectric constant (ϵ') measured at room temperature (298 K) for all samples studied. It can be observed that the studied samples exhibit high dielectric constants at low frequencies, which decreases with increasing frequency. Similar behavior was reported in some amorphous materials¹⁰⁷. Moreover, it can be noticed that the ϵ' is increased by doping TiO_2 and increasing its content. This behaviour can be explained based on the structural changes which produced the gradual formation of octahedral TiO_6 structural units by the incorporation of TiO_2 that cause the creation of defective dipoles within the glass network¹⁰⁸ in addition to introducing non-bridging oxygen atoms to the system that facilitate vibration of molecules/atoms¹⁰⁶. These can contribute to increased polarization under an applied electric field and consequently, the ϵ' is increased. These structural changes are confirmed by the FTIR study, which is in agreement with the above-mentioned discussion. It has been reported that the dielectric constant of materials depends on the dielectric properties of each phase, the concentration, and the interfaces between different phases^{107,109}. Therefore, the obtained results for glass ceramic samples BGC2 and BGC4 (Fig. 12b and Table 6) show the highest dielectric constant values due to the presence of BaTiO_3 phase (15%) in these samples, which were confirmed by XRD (Fig. 1b).

Also, in Fig. 12b, there are observed peaks at about 100 Hz for samples BGC2 and BGC4. These peaks may be due to the presence of crystalline phases and the formation of resonance frequency between the applied field and the interphase boundaries in these samples^{110,111}. Finally, the glass-ceramic exhibits a higher dielectric constant than the parent glass, suggesting the presence of interfacial polarization at the grain boundaries¹¹² and the ϵ' increases by the substitution of TiO_2 at the expense of BaO for all the investigated glasses and glass ceramic samples.

In Fig. 13, the dependence of dielectric loss tangent ($\tan \delta$) as a function of frequency for all the investigated glasses and glass ceramics is shown. From the figure, it is observed that the dielectric loss of the studied glass system increases with increasing TiO_2 , while the dielectric loss of the studied glass ceramics decreases with doping content. It has been reported that the higher the mobility of the conducting species, the higher the dielectric loss component^{113,114}, so the replacement of BaO by TiO_2 in the glasses leads to a more open and less strongly bonded network that tends to cause an increase in the dielectric losses¹¹⁵. But the more rigid structure caused by doping in the glass ceramics reveals the decrease in dielectric losses. In addition, the $\tan \delta$ remains approximately stable in the frequency range of 1–500 kHz. This behavior is beneficial for ceramics used in electrical energy storage^{116,117}.

Biological activities study

Antimicrobial activity

In general, the results in Table 7; Fig. 14 showed that glass ceramic had more antimicrobial activity than glass samples and this result is in accordance with those reported by Helmy et al.¹¹⁸ and Ouis et al.¹¹⁹. It was noticed that, as the concentration of TiO_2 content increased, the antimicrobial activity increased until definite

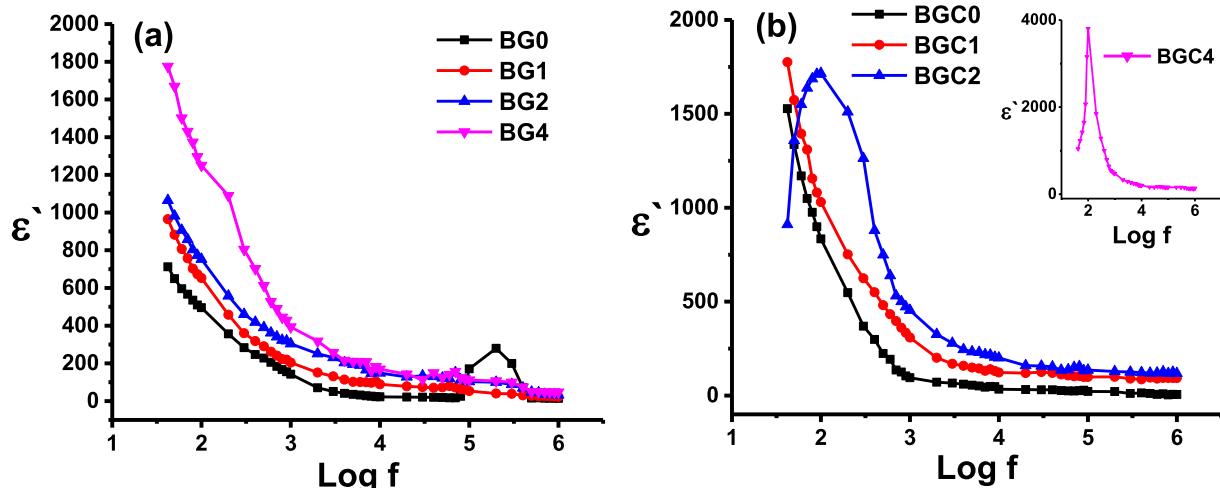


Fig. 12. Variation of dielectric constant (ϵ') as a function of frequency for all samples (a) glasses and (b) glass ceramics at room temperature.

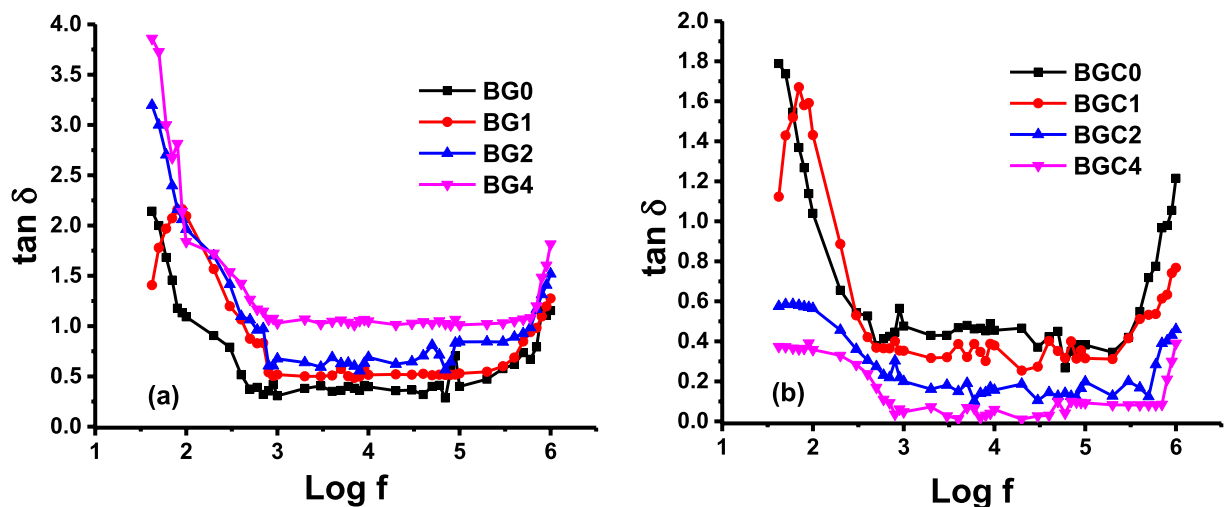


Fig. 13. Variation of dielectric loss ($\tan \delta$) as a function of frequency for all samples (a) glasses and (b) glass ceramics at room temperature.

Samples Code		Inhibition of microbial growth (%)				
		Microbes				
		<i>Bacillus cereus</i>	<i>Staphylococcus aureus</i>	<i>E. coli</i>	<i>Candida albicans</i>	<i>Aspergillus niger</i>
Glass	BG0	30.65 ± 0.12	12.45 ± 0.06	24.90 ± 0.46	-	-
	BG1	28.16 ± 0.33	22.18 ± 0.17	24.87 ± 0.69	-	-
	BG2	33.90 ± 0.52	18.29 ± 0.26	30.14 ± 0.27	-	-
	BG3	20.69 ± 0.58	14.59 ± 1.00	38.49 ± 0.84	-	-
	BG4	32.95 ± 0.16	17.12 ± 0.85	14.72 ± 0.65	12.60 ± 0.19	-
Glass ceramic	BGC0	52.76 ± 0.52	8.75 ± 0.65	-	7.35 ± 0.84	5.72 ± 0.44
	BGC1	59.00 ± 0.85	24.50 ± 0.84	-	24.00 ± 0.65	9.11 ± 0.19
	BGC2	60.43 ± 0.24	62.80 ± 0.24	-	39.30 ± 0.17	24.36 ± 1.05
	BGC3	64.03 ± 0.63	63.90 ± 0.49	-	30.67 ± 0.39	22.67 ± 1.22
	BGC4	56.83 ± 1.15	46.17 ± 0.64	-	15.02 ± 0.75	20.55 ± 0.99

Table 7. Antimicrobial activity of glass and glass ceramic samples (MIC).

concentration, after that, the activity decreased or still constant. Also, the antifungal activity against *Candida albicans* and *Aspergillus niger* and antibacterial activity against *Bacillus cereus* and *Staphylococcus aureus* of glass ceramic is preferable than glass samples, although the antimicrobial activity of glass against gram-negative bacteria (*E. coli*) was more than that of glass ceramic which had no activity against it, and this may be due to the hard structure of cell membrane of it. It was reported that boron components have antimicrobial activity against bacteria^{120,121} and fungi¹²². The antibacterial activity of boron may originate from its ability to rupture bacterial cell membranes through increasing release of free radicals (such as hydroxyl radicals $\cdot\text{OH}$) upon its reaction with H_2O ¹²³. Also, the antimicrobial effect may be related to an increase in pH in culture medium (alkaline medium) arising from alkaline ions release (such as sodium) and hence elevation of osmotic pressure attributable to glass dissolution^{124–126}. This increase in pH changes the integrity of the cytoplasmic membrane, promoting protein denaturation. The adjustment of intracellular pH might affect cellular functions, including the activity of enzymes essential for cellular metabolism¹²⁷. Concerning the small portion UV of the indoor natural light photocatalytic effect, the TiO_2 in borate glass generates reactive oxygen species (ROSSs) such as hydroxyl radical ($\cdot\text{OH}$), hydrogen peroxide (H_2O_2), superoxide radical anion (O_2^-) which cause oxidative damages to living organisms through lipid peroxidation of the cell membrane leading to the leach of proteins, minerals, and genetic materials¹²⁸. Incorporation of B atoms into the TiO_2 lattice (B-O-Ti as shown in FTIR) results in a charge imbalance and lattice distortion so TiO_2 generates surface oxygen vacancy, which also improves TiO_2 antimicrobial activity^{129,130}. From the obtained data of this study, it was observed the preferable antimicrobial activity of glass-ceramics than glass samples by increasing TiO_2 content. Our suggested assumption for this behavior is attributed to the thermal activation of TiO_2 at high temperatures. Nishikawa et al. verified experimentally the formation of oxygen vacancies in TiO_2 followed by the formation of trapped electrons and active radical species at high temperatures¹³¹. These oxygen vacancies and active radical species cause oxidative stress that can damage proteins, DNA, and lipids, resulting in microbial cell death^{129,132}. Finally,

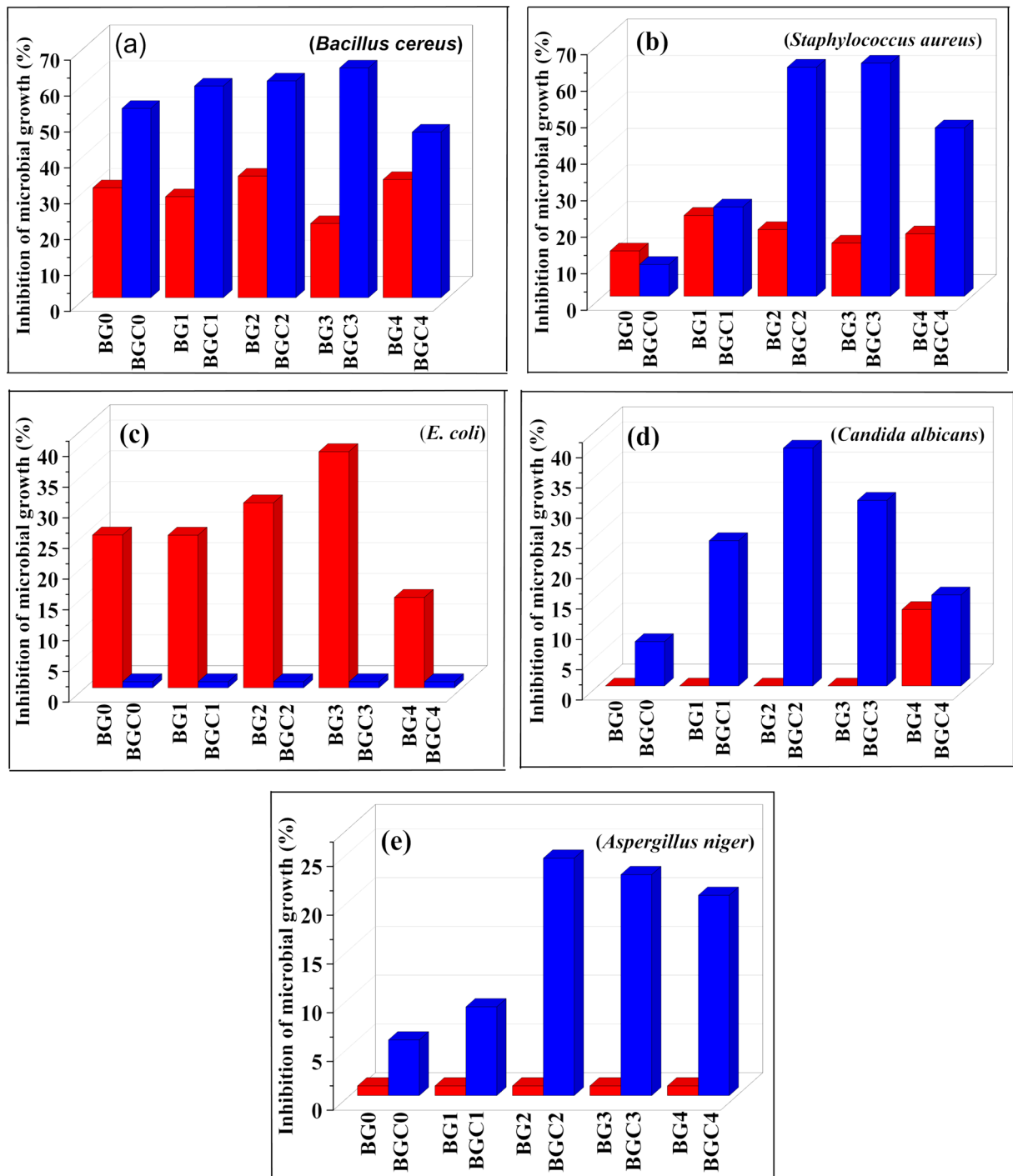


Fig. 14. Antimicrobial activity of glass and glass ceramic samples (MIC).

the enhanced antimicrobial activity is accounted for the synergistic effect of TiO_2 and B_2O_3 and these obtained results recommend samples for medical applications.

Longer-term stability assessments

The results observed in Table 8 indicated that the antimicrobial activity of samples stored for approximately one year remained nearly unchanged compared to freshly prepared samples. The glass ceramic was more stable than the glass, even after storage. These results recommended high stability of both glass and glass ceramic samples after approximately one year of storage where some samples of glass ceramic retained 100% of their activity after storage. The durability of the antimicrobial effect indicates the stability of the prepared glass and glass ceramics and the glass matrix successfully preserved its functionality So they are recommended in medical, pharmaceutical, and industrial applications.

Samples Code		Inhibition of microbial growth (%)					
		Microbes					
		<i>Bacillus cereus</i>	<i>Staphylococcus aureus</i>	<i>E. coli</i>	<i>Candida albicans</i>	<i>Aspergillus niger</i>	
Glass	BG0	49.62±0.12	5.98±1.23	-	4.87±0.55	3.25±0.14	
	BG1	55.21±0.32	22.55±0.26	-	20.63±0.74	5.37±0.85	
	BG2	57.36±0.57	60.70±0.47	-	31.31±0.96	20.63±0.99	
	BG3	60.15±1.00	64.54±0.87	-	20.35±0.21	15.69±0.41	
	BG4	53.24±1.06	45.12±0.64	-	11.23±0.32	12.00±1.20	
Glass ceramic	BGC0	48.56±0.32	49.20±0.74	17.21±0.54	25.63±1.32	14.20±0.45	
	BGC1	48.74±0.21	50.35±0.52	20.60±0.84	37.52±0.87	33.58±0.95	
	BGC2	50.00±0.52	58.14±0.14	28.63±0.41	50.54±1.11	45.32±0.74	
	BGC3	50.20±0.41	58.63±0.63	49.63±0.16	42.51±0.95	44.44±0.63	
	BGC4	55.21±0.98	60.00±0.99	22.41±0.10	34.62±0.12	18.32±0.21	

Table 8. Antimicrobial activity of glass and glass ceramic samples after storage on broth media.

Sample conc. (µg/ml)	Cell Viability %					
	Glass			Glass ceramics		
	BG0	BG2	BG4	BGC0	BGC2	BGC4
1000	21.05±2.13	38.61±2.35	24.59±2.17	23.46±1.68	14.78±1.26	11.42±0.84
500	45.13±2.71	49.85±1.74	47.21±1.43	46.78±2.05	39.57±1.91	30.61±1.25
250	76.91±1.45	88.04±0.82	80.69±1.85	79.24±1.48	62.35±1.83	48.19±1.76
125	92.40±0.68	99.72±0.17	94.13±0.69	92.95±0.71	86.04±1.27	78.65±1.23
62.5	98.17±0.46	100	98.96±0.22	99.04±0.13	93.76±0.62	91.34±0.29
31.25	100	100	100	100	99.86±0.39	98.12±0.64
15.6	100	100	100	100	100	100
7.8	100	100	100	100	100	100
0	100	100	100	100	100	100

Table 9. Values of cell Viability % with different concentrations of glass (BG0, BG2, and BG4) and glass ceramic (BGC0, BGC2, and BGC4) samples.

Cytotoxicity evaluation

Cell viability % of selected glass (BG0, BG2, and BG4) and their corresponding glass ceramic (BGC0, BGC2, and BGC4) samples was estimated in the cell culture media for 24 h against Human normal melanocytes cell line (HFB 4 cells) as shown in Table 9. The relation between cell viability % against different concentrations of glass and glass ceramics (7.8–1000 µg/ml) is plotted to get the survival curve of the tested cell line after treatment with samples (Fig. 15). The cytotoxicity concentration CC_{50} , the concentration required to cause toxic effects in 50% of intact cells, was also demonstrated in Fig. 15. As demonstrated, the cell viability was affected by both the concentrations of the samples and the content of TiO_2 . It is worth mentioning that all synthesized glass and glass ceramics exhibit approximately 100% cell viability at concentrations ranging from 7.8 to 31.25 µg/ml and (91.34–99.72%) cell viability at concentrations up to 125 µg/ml (except for BGC2 and BGC4). Unlike results reported in¹³³, the glass samples have minimal cytotoxicity compared with their corresponding glass ceramics. The values of cell viability obtained in this study are good compared to the cell viability values reported in¹³³. It can be confirmed that the prepared glass and glass ceramics samples were nontoxic in nature, because the cell viability is greater than 70%⁴⁷ so, these results suggest that the glass and glass-ceramic samples had lower to normal cytotoxicity at concentration up to 250 µg/ml (except the BGC2 and BGC4 samples that had lower cytotoxicity at concentration up to 125 µg/ml) and could be safely used as biocompatible materials.

Conclusion

Briefly, a series of TiO_2 -modified borate glass compositions (40 B_2O_3 -20 Al_2O_3 -10 NaF-(30-X) BaO-X TiO_2) where, (0≤X≤2.5) mol% were prepared by melt quench method to study the effect of gradual addition of TiO_2 at expense of BaO on structural, electrical and antimicrobial properties. Also, the corresponding glass-ceramics were synthesized by heat treatment at a nucleation temperature of 480°C for 4 h and a crystal growth temperature of 750°C with a rate of 5 °C/min for 6 h. FTIR study showed the appearance of titanium ions in the network of the glass, mainly as TiO_4 (network former) at lower concentrations of TiO_2 and TiO_6 (network modifier) with a gradual increase in TiO_2 content. For glass-ceramics, FTIR showed sharp and split peaks due to the fine crystalline derivatives, which were also confirmed by XRD and SEM measurements. A slight decrease in density from 3.494 g/cm³ to 3.273 g/cm³ and an expansion in the molar volume from 28.173cm³/mol to 29.627cm³/mol were caused as a result of the substitution of BaO by TiO_2 in the glass network. The electrical conductivity of the

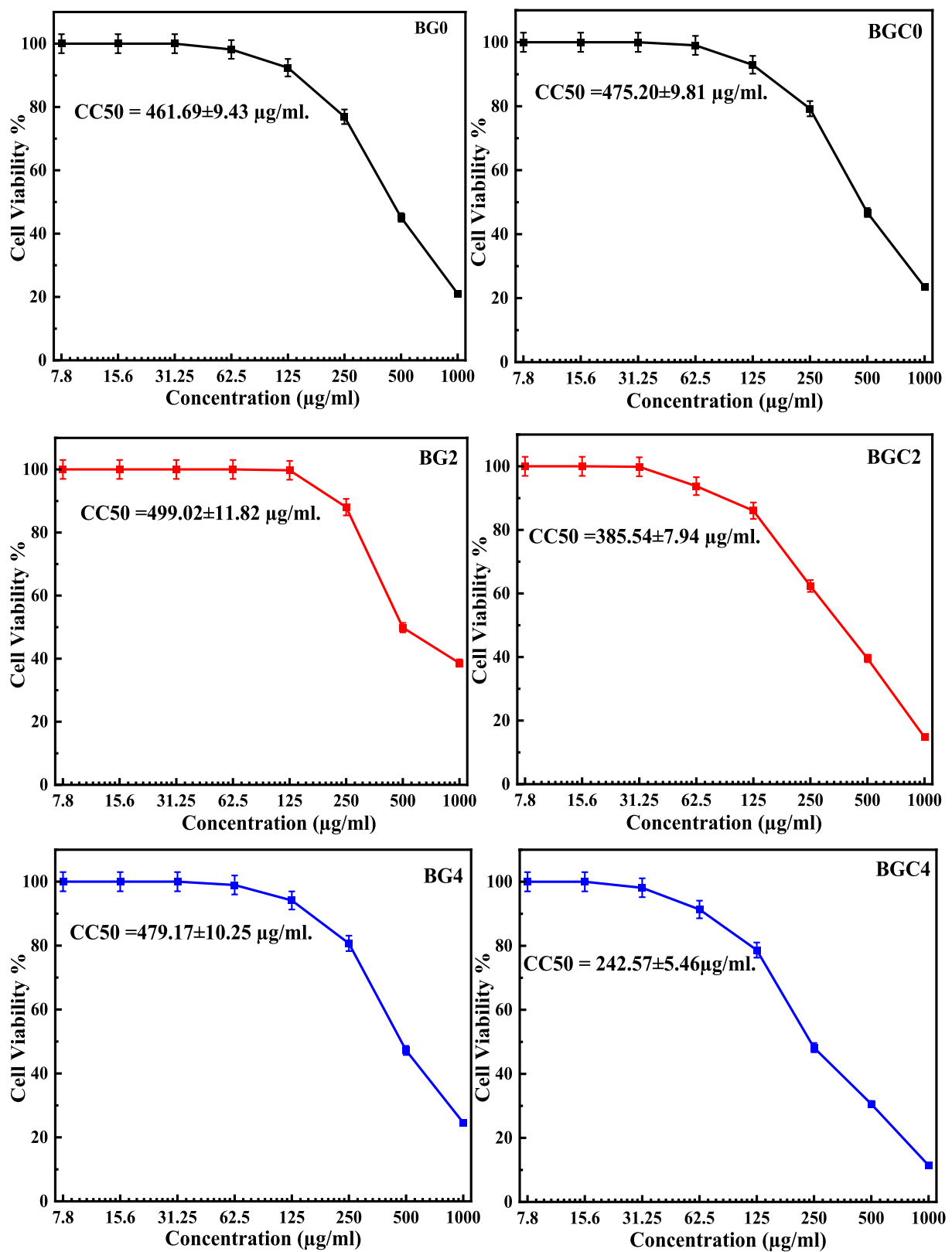


Fig. 15. Effect of different concentrations of glass (BG0, BG2, and BG4) and glass ceramic (BGC0, BGC2, and BGC4) samples on Cell Viability % and CC_{50} .

glass and glass ceramics is thermally activated and follows Arrhenius' behaviour. The calculated activation energy lies in the range of 0.053–0.728 (eV) and 0.037 – 0.462 (eV) for glass and glass ceramic samples, respectively. The DC conductivity values of the studied samples indicated that the incorporation of TiO_2 results in higher conductivity values than those of the free samples. The prepared glasses doped with TiO_2 and its glass ceramics exhibited a semiconducting nature and the magnitude of the σ_{dc} values indicated that the electrical conductivity of such samples lies in the range of semiconductors. The glass-ceramic exhibits higher dielectric constants than the parent glass, and it increases by doping with TiO_2 . Due to values of electrical conductivity and ϵ' , the present samples can be considered as good candidates for energy storage and are one of the semiconductor categories that can be used in electronic devices. The prepared doped- TiO_2 borate glass and glass ceramics were found to have biological activity against various species of microbes, but glass ceramic is more preferable than the parent one. The results recommended high stability of both glass and glass ceramic samples after approximately one year of storage. The prepared glass and glass ceramics samples were nontoxic in nature and the glass samples have minimal cytotoxicity compared with their corresponding glass ceramics. Finally, the unique fabrication of promising multifunctional materials of TiO_2 -doped borate glasses and glass-ceramics can meet the demands of both biological and electrical applications.

Data availability

Availability of Data & Materials The data of this work is available for any person after publication. For any questions about the data from this study contact the corresponding author (Gehad Y. Abo El-Reesh).

Received: 13 March 2025; Accepted: 19 May 2025

Published online: 03 June 2025

References

- Walia, T. & Singh, K. Mixed alkaline Earth modifiers effect on thermal, optical and structural properties of $\text{SrO}\text{-}\text{BaO}\text{-}\text{SiO}_2\text{-}\text{B}_2\text{O}_3\text{-}\text{ZrO}_2$ glass sealants. *J. Non-cryst. Solids.* **564**, 120812 (2021).
- Kaur, N., Kaur, G., Kumar, D. & Singh, K. Mechanical and thermal properties of $\text{SrO}\text{/BaO}$ modified $\text{Y}_2\text{O}_3\text{-}\text{Al}_2\text{O}_3\text{-}\text{B}_2\text{O}_3\text{-}\text{SiO}_2$ glasses and their compatibility with solid oxide fuel cell components. *J. Phys. Chem. Solids.* **118**, 248–254 (2018).
- Kroug-Moe, J. Interpretation of infrared spectra of Boron oxide and alkali Borate glasses. *Phys. Chem. Glasses.* **2**, 46 (1965).
- Griscom, D. L. *In Borate Glasses: Structure, Properties, Applications* 11–138 (Springer, 1978).
- Ezz-Eldin, F. M. Leaching and mechanical properties of cabal glasses developed as matrices for immobilization high-level wastes. *Nucl. Instrum. Methods Phys. Res. Sect. B.* **183**, 285–300 (2001).
- Ojovan, M. I. & Lee, W. E. Glassy wasteforms for nuclear waste immobilization. *Metall. Mater. Trans. A.* **42**, 837–851 (2011).
- Tuller, H. L., Button, D. P. & Uhlmann, D. R. Fast ion transport in oxide glasses. *J. Non-cryst. Solids.* **40**, 93–118 (1980).
- Samuneva, B., Bozadjiev, P., Djambaski, P. & Rangelova, N. Borate agriglasses: Synthesis and application. *Glass Technol.* **41**, 206–208 (2000).
- Hassaan, M. Y., Osman, H. M., Hassan, H. H., El-Deeb, A. S. & Helal, M. A. Optical and electrical studies of borosilicate glass containing vanadium and Cobalt ions for smart windows applications. *Ceram. Int.* **43**, 1795–1801 (2017).
- Zaman, F. et al. Investigation of luminescence and laser transition of Dy^{3+} in $\text{Li}_2\text{O}\text{-}\text{Gd}_2\text{O}_3\text{-}\text{Bi}_2\text{O}_3\text{-}\text{B}_2\text{O}_3$ glasses. *Opt. Mater.* **55**, 136–144 (2016).
- Mancuso, E., Bretcanu, O., Marshall, M. & Dalgarno, K. W. Sensitivity of novel silicate and borate-based glass structures on in vitro bioactivity and degradation behaviour. *Ceram. Int.* **43**, 12651–12657 (2017).
- Simila, H. O. & Boccaccini, A. R. Sol-gel bioactive glass containing biomaterials for restorative dentistry: A review. *Dent. Mater.* **38**, 725–747 (2022).
- Pant, G., Krishna, B. V., Abed, Nagpal, N. & Meheta A. A. 01026 (EDP Sciences).
- Kargoza, S., Montazerian, M., Fiume, E. & Baino, F. Multiple and promising applications of strontium (Sr)-containing bioactive glasses in bone tissue engineering. *Front. Bioeng. Biotechnol.* **7**, 161 (2019).
- Piatti, E., Miola, M. & Verné, E. Tailoring of bioactive glass and glass-ceramics properties for in vitro and in vivo response optimization: A review. *Biomater. Sci.* (2024).
- Brown, R. F. et al. Effect of Borate glass composition on its conversion to hydroxyapatite and on the proliferation of MC3T3-E1 cells. *J. Biomed. Mater. Res. Part. A Off. J. Soc. Biomater. Jpn. Soc. Biomater. Aust. Soc. Biomater. Korean Soc. Biomater.* **88**, 392–400 (2009).
- Huang, W., Day, D. E., Kittiratanapiboon, K. & Rahaman, M. N. Kinetics and mechanisms of the conversion of silicate (45S5), Borate, and borosilicate glasses to hydroxyapatite in dilute phosphate solutions. *J. Mater. Sci. Mater. Med.* **17**, 583–596 (2006).
- Ege, D., Zheng, K. & Boccaccini, A. R. Borate bioactive glasses (BBG): Bone regeneration, wound healing applications, and future directions. *ACS Appl. Biol. Mater.* **5**, 3608–3622 (2022).
- Chen, R. et al. Nanosized HCA-coated Borate bioactive glass with improved wound healing effects on rodent model. *Chem. Eng. J.* **426**, 130299 (2021).
- Ottomeyer, M., Mohammadkhan, A., Day, D. E. & Westenberg, D. J. Broad-spectrum antibacterial characteristics of four novel borate-based bioactive glasses. (2016).
- da Silva, G. L. et al. Bioactive antibacterial Borate glass and glass-ceramics. *J. Non-cryst. Solids.* **595**, 121829 (2022).
- Datta, S. et al. Effect of Boron oxide addition on structural, thermal, in vitro bioactivity and antibacterial properties of bioactive glasses in the base S53P4 composition. *J. Non-cryst. Solids.* **498**, 204–215 (2018).
- Plewinski, M. et al. The effect of crystallization of bioactive bioglass 45S5 on apatite formation and degradation. *Dent. Mater.* **29**, 1256–1264 (2013).
- Thavornyutikarn, B., Feltis, B., Wright, P. F. A. & Turney, T. W. Effect of pre-treatment of crystallized bioactive glass with cell culture media on structure, degradability, and biocompatibility. *Mater. Sci. Eng. C.* **97**, 188–197 (2019).
- Li, H. C., Wang, D. G., Hu, J. H. & Chen, C. Z. Crystallization, mechanical properties and in vitro bioactivity of sol-gel derived $\text{Na}_2\text{O}\text{-}\text{CaO}\text{-}\text{SiO}_2\text{-}\text{P}_2\text{O}_5$ glass-ceramics by partial substitution of CaF_2 for CaO . *J. Solgel Sci. Technol.* **67**, 56–65 (2013).
- Heras, C. et al. Multifunctional antibiotic-and zinc-containing mesoporous bioactive glass scaffolds to fight bone infection. *Acta Biomater.* **114**, 395–406 (2020).
- Anand, A. et al. Influence of copper-strontium co-doping on bioactivity, cytotoxicity and antibacterial activity of mesoporous bioactive glass. *Gels* **8**, 743 (2022).
- Fakher, S. & Westenberg, D. Properties and antibacterial effectiveness of metal-ion doped borate-based bioactive glasses. *Fut. Microbiol.*, 1–17 (2025).
- Liu, Y. et al. Effective antibacterial activity of degradable copper-doped phosphate-based glass nanozymes. *ACS Appl. Mater. Interfaces.* **13**, 11631–11645 (2021).

30. Abodunrin, O. D., Mabrouk, E., Bricha, M. & K. & A review on Borate bioactive glasses (BBG): Effect of doping elements, degradation, and applications. *J. Mater. Chem. B* **11**, 955–973 (2023).
31. Shaaban, K. S., Yousef, E. S., Mahmoud, S. A., Wahab, E. A. A. & Shaaban, E. R. Mechanical, structural and crystallization properties in titanate doped phosphate glasses. *J. Inorg. Organomet. Polym. Mater.* **30**, 4655–4663 (2020).
32. Shaaban, K. S., Wahab, E. A. A., Shaaban, E. R., Yousef, E. S. & Mahmoud, S. A. Electronic polarizability, optical basicity, thermal, mechanical and optical investigations of $(65\text{B}_2\text{O}_3-30\text{Li}_2\text{O}-5\text{Al}_2\text{O}_3)$ glasses doped with titanate. *J. Electron. Mater.* **49**, 2040–2049 (2020).
33. Gomaa, H. M., Elkatlawy, S. M., Yahia, I. S., Saudi, H. A. & Abdel-Ghany, A. M. Influence of the gradual increase of TiO_2 -impurities on the structural and optical properties of some calcium sodium Borate glasses. *Optik* **244**, 167543 (2021).
34. Bamford, C. Colour generation and control in glass. (No Title) (1977).
35. Abdelghany, A. M. & ElBatal, H. A. Effect of TiO_2 doping and gamma ray irradiation on the properties of $\text{SrO-B}_2\text{O}_3$ glasses. *J. Non-cryst. Solids.* **379**, 214–219 (2013).
36. Shaim, A. & Et-Tabirou, M. Role of titanium in sodium titanophosphate glasses and a model of structural units. *Mater. Chem. Phys.* **80**, 63–67 (2003).
37. Es-Soufi, H. & Bih, L. Effect of TiO_2 on the chemical durability and optical properties of Mo-based phosphate glasses. *J. Non-cryst. Solids.* **558**, 120655 (2021).
38. Biswas, K., Sontakke, A. D. & Annapurna, K. Effect of TiO_2 on thermal, structural and third-order nonlinear optical properties of Ca-La-B-O glass system. *J. Alloys Compd.* **489**, 493–498 (2010).
39. Back, G. S., Yoon, M. J. & Jung, W. G. Effect of the Cr_2O_3 and TiO_2 as nucleating agents in $\text{SiO}_2\text{-Al}_2\text{O}_3\text{-CaO-MgO}$ glass-ceramic system. *Met. Mater. Int.* **23**, 798–804 (2017).
40. Morige, R. et al. Influence of the porosity and type of bioglass on the micro-mechanical and bioactive behavior of coated porous titanium substrates. *J. Non-cryst. Solids.* **551**, 120436 (2021).
41. Schumacher, M., Habibovic, P. & Van Rijt, S. Mesoporous bioactive glass composition effects on degradation and bioactivity. *Bioactive Mater.* **6**, 1921–1931 (2021).
42. El-Kady, A. M., Kamel, N. A., Elnashar, M. M. & Farag, M. M. Production of bioactive Glass/chitosan scaffolds by freeze-gelation for optimized Vancomycin delivery: effectiveness of glass presence on controlling the drug release kinetics. *J. Drug Deliv. Sci. Technol.* **66**, 102779 (2021).
43. Naseri, S., Lepry, W. C. & Nazhat, S. N. Bioactive glasses in wound healing: Hope or hype? *J. Mater. Chem. B* **5**, 6167–6174 (2017).
44. Chouirfa, H., Bouloussa, H., Migonney, V. & Falentin-Daudré, C. Review of titanium surface modification techniques and coatings for antibacterial applications. *Acta Biomater.* **83**, 37–54 (2019).
45. Ferraris, S. & Spriano, S. Antibacterial titanium surfaces for medical implants. *Mater. Sci. Eng. C* **61**, 965–978 (2016).
46. Shafaghi, R. et al. Effect of TiO_2 doping on degradation rate, microstructure and strength of Borate bioactive glass scaffolds. *Mater. Sci. Eng. C* **107**, 110351 (2020).
47. Samudrala, R., Penuguri, V. & Manayathi, B. Cytocompatibility studies of titania-doped calcium borosilicate bioactive glasses in-vitro. *Mater. Sci. Eng. C* **77**, 772–779 (2017).
48. Mao, H. et al. Design of a $\text{BaO-Al}_2\text{O}_3\text{-SiO}_2\text{-B}_2\text{O}_3$ glass-ceramic for microwave LTCC substrate material based on glass-ceramic + ceramic composite. *J. Mater. Sci. Mater. Electron.* **33**, 24834–24844 (2022).
49. Raheja, S., Singh, R. & Uddin, M. Electrical characterization of sodium cadmium Borate glasses doped with TiO_2 . *J. Inst. Eng. (India) Ser. D* **103**, 497–503 (2022).
50. El Yousef, S., SayedMostafa, E. & El-Adawy, A. Optical and electrical properties of Borate glasses in the system: $\text{B}_2\text{O}_3/\text{Na}_2\text{O}/\text{TiO}_2$. *J. Appl. Sci.* **6**, 1292–1297 (2006).
51. Al Kiey, S. A., Abdel-Hameed, S. A. M. & Marzouk, M. A. Influence of transition metals on the development of semiconducting and low thermal expansion TiO_2 -borosilicate glasses and glass ceramics. *Silicon* **16**, 2945–2953 (2024).
52. Mohamed, S. N., Halimah, M. K., Subban, R. H. Y. & Yahya, A. K. AC conductivity and dielectric properties in mixed ionic-electronic $20\text{Na}_2\text{O-20CaO-(60-x)B}_2\text{O}_3\text{-xV}_2\text{O}_5$ glasses. *Phys. B Condens. Matter.* **602**, 412480 (2021).
53. Patial, B. S., Prakash, J., Kumar, R., Tripathi, S. K. & Thakur, N. Dielectric properties and AC conductivity measurements of amorphous Ge15Se85 glass. (2013).
54. Osés, S. M. et al. Comparison of methods to determine antibacterial activity of honeys against *Staphylococcus aureus*. *NJAS-Wageningen J. Life Sci.* **78**, 29–33 (2016).
55. Son, S. & Kim, K. Effect of TiO_2 content on crystallization behavior of $\text{CaO-Al}_2\text{O}_3\text{-SiO}_2\text{-ZnO}$ glass-ceramic glaze. *Ceram. Int.* **49**, 13677–13686 (2023).
56. Zhang, B. et al. The effect of TiO_2 and B_2O_3 on sintering behavior and crystallization behavior of $\text{SrO-BaO-B}_2\text{O}_3\text{-SiO}_2$ glass-ceramics. *Ceram. Int.* **48**, 7013–7023 (2022).
57. Kamitsos, E. I., Patsis, A. P. & Chryssikos, G. D. Infrared reflectance investigation of alkali borate glasses. *J. Non-cryst. Solids.* **152**, 246–257 (1993).
58. Ciceo-Lucacel, R. & Ardelean, I. FT-IR and Raman study of silver lead borate-based glasses. *J. Non-cryst. Solids.* **353**, 2020–2024 (2007).
59. Varsamis, C. P., Kamitsos, E. I. & Chryssikos, G. D. Spectroscopic investigation of AgI-doped Borate glasses. *Solid State Ionics.* **136**, 1031–1039 (2000).
60. Sun, Y. & Zhang, Z. Structural roles of Boron and silicon in the $\text{CaO-SiO}_2\text{-B}_2\text{O}_3$ glasses using FTIR, Raman, and NMR spectroscopy. *Metall. Mater. Trans. B* **46**, 1549–1554 (2015).
61. El Batal, F. H., Kheshen, E., Abooz, A. A., Abo-Naf, S. M. & M. A. & Gamma ray interaction with lithium borate glasses containing transition metals ions. *Opt. Mater.* **30**, 881–891 (2008).
62. Marzouk, M. A., ElBatal, F. H. & ElBatal, H. A. Effect of TiO_2 on the optical, structural and crystallization behavior of barium Borate glasses. *Opt. Mater.* **57**, 14–22 (2016).
63. Abdelghany, A. M. & Behairy, A. Optical parameters, antibacterial characteristics and structure correlation of copper ions in cadmium Borate glasses. *J. Mater. Res. Technol.* **9**, 10491–10497 (2020).
64. Kamitsos, E. I. Infrared studies of Borate glasses. *Phys. Chem. Glasses.* **44**, 79–87 (2003).
65. Raju, G. N., Rao, P. V., Kumar, V. R., Chandrakala, C. & Ashok, J. Study on the influence of TiO_2 on the characteristics of multi component modifier oxide based B_2O_3 glass system. *J. Non-cryst. Solids.* **498**, 309–314 (2018).
66. Alajerami, Y. S. M., Hashim, S., Hassan, W. M. S. W. & Ramli, A. T. The effect of titanium oxide on the optical properties of lithium potassium Borate glass. *J. Mol. Struct.* **1026**, 159–167 (2012).
67. Sigaev, V. N. et al. Structure of lead Germanate glasses by Raman spectroscopy. *J. Non-cryst. Solids.* **279**, 136–144 (2001).
68. Abdelghany, A. M., Ouis, M. A., Abooz, M. A., ElBatal, H. A. & El-Bassyouni, G. T. Role of SrO on the bioactivity behavior of some ternary Borate glasses and their glass ceramic derivatives. *Spectrochim. Acta Part A Mol. Biomol. Spectrosc.* **152**, 126–133 (2016).
69. Doweidar, H. & Saddeek, Y. B. FTIR and ultrasonic investigations on modified bismuth Borate glasses. *J. Non-cryst. Solids.* **355**, 348–354 (2009).
70. Kamitsos, E. I., Patsis, A. P., Karakassides, M. A. & Chryssikos, G. D. Infrared reflectance spectra of lithium Borate glasses. *J. Non-Cryst. Solids.* **126**, 52–67 (1990).
71. Rao, R. B., Rao, D. K. & Veeraiah, N. The role of titanium ions on structural, dielectric and optical properties of $\text{Li}_2\text{O-MgO-B}_2\text{O}_3$ glass system. *Mater. Chem. Phys.* **87**, 357–369 (2004).

72. Raghavaiah, B. V., Laxmikanth, C. & Veeraiah, N. Spectroscopic studies of titanium ions in $\text{PbO-Sb}_2\text{O}_3\text{-As}_2\text{O}_3$ glass system. *Opt. Commun.* **235**, 341–349 (2004).
73. Elsagher, H. M. et al. The influence of Er^{3+} ions on the spectroscopic and lasing characteristics of alkaline Earth titanium Borate glasses for photonic applications. *Opt. Mater.* **131**, 112624 (2022).
74. Azooz, M. A. & ElBatal, H. A. Preparation and characterization of invert $\text{ZnO-B}_2\text{O}_3$ glasses and its shielding behavior towards gamma irradiation. *Mater. Chem. Phys.* **240**, 122129 (2020).
75. Saddeek, Y. B., Aly, K. A., Shaaban, K. S., Ali, A. M. & Sayed, M. A. The effect of TiO_2 on the optical and mechanical properties of heavy metal oxide borosilicate glasses. *Silicon* **11**, 1253–1260 (2019).
76. Farouk, M. Effect of TiO_2 on the structural, thermal and optical properties of $\text{BaO-Li}_2\text{O}$ -diborate glasses. *J. Non-cryst. Solids.* **402**, 74–78 (2014).
77. Es-Soufi, H., Bih, L., Manoun, B. & Lazor, P. Structure, thermal analysis and optical properties of lithium tungsten-titanophosphate glasses. *J. Non-Cryst. Solids.* **463**, 12–18 (2017).
78. Shaaban, K. S. Optical properties of Bi_2O_3 doped Boro tellurite glasses and glass ceramics. *Optik* **203**, 163976 (2020).
79. Shaaban, K. S., Yousef, E. S., Abdel Wahab, E. A., Shaaban, E. R. & Mahmoud, S. A. Investigation of crystallization and mechanical characteristics of glass and glass-ceramic with the compositions $\text{X Fe}_2\text{O}_3\text{-35SiO}_2\text{-35B}_2\text{O}_3\text{-10Al}_2\text{O}_3\text{-(20-x) Na}_2\text{O}$. *J. Mater. Eng. Perform.* **29**, 4549–4558 (2020).
80. Song, C. H., Choi, H. W., Kim, M., Jin, G. Y. & Yang, Y. S. Electrical relaxations of amorphous $\text{xKNbO}\sim 3$ ($1-\text{x}$) $\text{SiO}\sim 2$ ($\text{x}=0.33, 0.5, 0.67, 0.8$). *J.-Kor. Phys. Soc.* **51**, 674 (2007).
81. Gomaa, M. M., Abo-Mosallam, H. A. & Darwish, H. Electrical and mechanical properties of alkali barium titanium aluminoborosilicate glass-ceramics containing strontium or magnesium. *J. Mater. Sci. Mater. Electron.* **20**, 507–516 (2009).
82. Shaaban, M. H. The ac conductivity of CuO -containing lead silicate glasses. *J. Mater. Sci. Mater. Electron.* **9**, 55–60 (1998).
83. Margha, F. H., El-Bassyouni, G. T. & Turky, G. M. Enhancing the electrical conductivity of vanadate glass system (Fe_2O_3 , B_2O_3 , V_2O_5) via doping with sodium or strontium cations. *Ceram. Int.* **45**, 11838–11843 (2019).
84. Moustafa, M. G. Electrical transport properties and conduction mechanisms of semiconducting iron bismuth glasses. *Ceram. Int.* **42**, 17723–17730 (2016).
85. Das, A. S. & Biswas, D. Investigation of ac conductivity mechanism and dielectric relaxation of semiconducting neodymium-vanadate nanocomposites: Temperature and frequency dependency. *Mater. Res. Express.* **6**, 075206 (2019).
86. Gustian, I. et al. Synthesis of polymer electrolyte membrane based on acid-base complex pair and its characteristics. *J. Math. Fund. Sci.* **46**, 50–61 (2014).
87. Banagar, A. V., Kumar, M. B., Nagaraja, N., Tipperudra, A. & Jakati DC electrical conduction in strontium vanadium Borate glasses. *Mater. Sci.* **38**, 359–366 (2020).
88. Belkhououi, C., Lefi, R., Mzabi, N. & Smaoui, H. Synthesis, optical and electrical properties of Mn doped ZnO nanoparticles. *J. Mater. Sci. Mater. Electron.* **29**, 7020–7031 (2018).
89. Al-Hajry, A., Soliman, A. A. & El-Desoky, M. M. Electrical and thermal properties of semiconducting $\text{Fe}_2\text{O}_3\text{-Bi}_2\text{O}_3\text{-Na}_2\text{B}_4\text{O}_7$ glasses. *Thermochim. Acta* **427**, 181–186 (2005).
90. Anwar, M., Ghauri, I. M. & Siddiqi, S. A. The electrical properties of amorphous thin films of $\text{Al-In}\sim 20\sim 3\text{-Al}$ structure deposited by thermal evaporation. *Rom. J. Phys.* **50**, 763 (2005).
91. Kishore, N. & Agarwal, A. Study of structural, optical and transport properties of semiconducting $\text{Fe}_2\text{O}_3\text{-PbO-B}_2\text{O}_3$ glasses. (2010).
92. Singh, A., Prasad, K. & Prasad, A. Effects of Sr^{2+} doping on the electrical properties of $(\text{Bi}_{0.5}\text{Na}_{0.5})\text{0.94 Ba}_{0.06}\text{TiO}_3$ ceramics. *Process. Appl. Ceram.* **9**, 33–42 (2015).
93. Sharma, V. et al. Conductivity relaxation and oxygen vacancies-related electron hopping mechanism in $\text{Pb}_{1-x}\text{La}_{x}\text{Sm}_{2\text{x}}/2\text{Ti}_{1-x}\text{Fe}_{\text{x}}\text{O}_3$ solid solutions. *J. Asian. Ceram. Soc.* **6**, 222–231 (2018).
94. Shapaa, M. Structure and electric conductivity of mixed Electronic-Ionic $\text{Bi}_2\text{O}_3\text{-Li}_2\text{O-V}_2\text{O}_5\text{-B}_2\text{O}_3$ glass system. *Int. J. Thin Fil. Sci. Tec.* **6**, 45–52 (2017).
95. Rani, S., Sanghi, S., Agarwal, A., Kishore, N. & Seth, V. P. Effect of ZnO/CdO on the structure and electrical conductivity in $\text{Li}_2\text{O}\text{-MO-Bi}_2\text{O}_3\text{-B}_2\text{O}_3$ glasses ($\text{M}=\text{Zn, Cd}$). *J. Phys. Chem. Solids.* **69**, 1855–1860 (2008).
96. Kundu, V., Dhiman, R. L., Maan, A. S., Goyal, D. R. & Arora, S. Characterization and electrical conductivity of vanadium doped strontium bismuth Borate glasses. *J. Optoelectron. Adv. Mater.* **12**, 2373 (2010).
97. Cizman, A. et al. The effect of Fe on the structure and electrical conductivity of sodium borosilicate glasses. *Phys. Chem. Chem. Phys.* **19**, 23318–23324 (2017).
98. Vaish, R. & Varma, K. B. R. Dielectric behavior of sodium Borate glasses. *Ionics* **17**, 727–731 (2011).
99. Gundale, S. S., Behare, V. V. & Deshpande, A. V. Study of electrical conductivity of $\text{Li}_2\text{O-B}_2\text{O}_3\text{-SiO}_2\text{-Li}_2\text{SO}_4$ glasses and glass-ceramics. *Solid State Ionics* **298**, 57–62 (2016).
100. Khater, G. A., Nabawy, B. S., Kang, J. & Mahmoud, M. A. Dielectric properties of basaltic glass and glass-ceramics: Modeling and applications as insulators and semiconductors. *Silicon* **11**, 579–592 (2019).
101. Suhail, M. H., Essa, A. & Ahmed, R. A. I. M. AC conductivity and dielectric study of doped ZnS thin films prepared by chemical spray pyrolysis.
102. Es-Soufi, H., Bih, L. & Benzineb, M. Study of tungsten phosphate glasses containing Fe_2O_3 . *New. J. Glass Ceram.* **9**, 33–49 (2019).
103. Bahgat, A. A. & Abou-Zeid, Y. M. Mixed alkali effect in the $\text{K}_2\text{O-Na}_2\text{O-TeO}_2$ glass system. *Phys. Chem. Glasses* **42**, 361–370 (2001).
104. Megha, U., Varghese, G. & Shijina, K. Room temperature AC impedance and dielectric studies of Bi and Sr doped $\text{PrCo}_{0.6}\text{Fe}_{0.4}\text{O}_3$ perovskites. *Process. Appl. Ceram.* **11**, 52–59 (2017).
105. Goswami, M., Deshpande, S. K., Kumar, R. & Kothiyal, G. P. Electrical behaviour of $\text{Li}_2\text{O-ZnO-SiO}_2$ glass and glass-ceramics system. *J. Phys. Chem. Solids.* **71**, 739–744 (2010).
106. Morsi, R. M. M., El-Ghany, A., Morsi, M. M. & S. I. & Electrical properties of silicate glasses of low level gadolinium oxide doping including dielectric and infrared measures. *J. Mater. Sci. Mater. Electron.* **26**, 1419–1426 (2015).
107. Margha, F. H., Morsi, R. M. M. & Hamzawy, E. M. A. Characterization and electrical properties of tausonite (SrTiO_3) in nano ceramic composites. *J. Mater. Sci. Mater. Electron.* **30**, 16257–16265 (2019).
108. Hu, W., Li, L., Li, G., Liu, Y. & Withers, R. L. Atomic-scale control of TiO_6 octahedra through solution chemistry towards giant dielectric response. *Sci. Rep.* **4**, 6582 (2014).
109. Jin, S. et al. Dielectric properties of modified $\text{SrTiO}_3/\text{PTFE}$ composites for microwave RF antenna applications. *J. Mater. Sci. Mater. Electron.* **26**, 7431–7437 (2015).
110. Morsi, R. M. M., Basha, M. A. F. & Morsi, M. M. Synthesis and physical characterization of amorphous silicates in the system $\text{SiO}_2\text{-Na}_2\text{O-RO}$ ($\text{R}=\text{Zn, Pb or Cd}$). *J. Non-Cryst. Solids.* **439**, 57–66 (2016).
111. Mahde, D. K., Chiad, B. T. & Mohamed, G. H. Evaluation of ac conductivity for lead silicate glass from dielectric measurements. *J. Electron. Devices.* **12**, 750–775 (2012).
112. Zhang, Y., Wang, X. R., Song, X. Z., Ma, T. & Zhang, Q. Interfacial polarization arising from two contributions in glass added barium titanate ceramics. *J. Mater. Sci. Mater. Electron.* **23**, 2301–2305 (2012).
113. Reddy, C. P., Naresh, V., Ramaraghavulu, R., Rudramadevi, B. H. & Buddhudu, S. Optical and dielectric properties of cr 3 & Cu 2: $\text{P}_2\text{O}_5\text{-ZnO-LiF}$ glasses.
114. Ingram, M. D. Ionic conductivity in glass. *Phys. Chem. Glasses* **28**, 215–234 (1987).

115. McMillan, P. W. The crystallisation of glasses. *J. Non-cryst. Solids.* **52**, 67–76 (1982).
116. Wang, X. W. et al. Enhanced energy storage properties in $\text{Ba}_{0.85}\text{Ca}_{0.15}\text{Zr}_{0.1}\text{Ti}_{0.9}\text{O}_3$ ceramics with glass additives. *J. Appl. Phys.* **127** (2020).
117. Du, X. et al. Optimizing the energy storage performance of $\text{K}_2\text{O}-\text{Nb}_{2}\text{O}_5-\text{SiO}_2$ based glass-ceramics with excellent temperature stability. *Ceram. Int.* **47**, 8987–8995 (2021).
118. Helmy, A. K. et al. Preparation and characterization of some composite phosphate glass-polyaniline derivatives studying their antimicrobial activity. *Egypt. J. Chem.* **64**, 5315–5326 (2021).
119. Ouis, M. & Gamal, A. Role of silver ions in $\text{Na}_2\text{O}-\text{CaF}_2-\text{P}_2\text{O}_5$ host glass and its corresponding glass-ceramic: Searching for antibacterial behaviour-supplemented by spectral, optical, FTIR and SEM investigations. *Egypt. J. Chem.* **64**, 5345–5355 (2021).
120. Celebi, O. et al. Antibacterial activity of Boron compounds against biofilm-forming pathogens. *Biol. Trace Elem. Res.* **202**, 346–359 (2024).
121. Kilic, A., Beyazsakal, L., Findik, B. T. & Incebay, H. Synthesis and electrochemical investigation of chiral amine Bis (phenolate)-boron complexes: In vitro antibacterial activity screening of Boron compounds. *Inorg. Chim. Acta.* **510**, 119777 (2020).
122. Du, S. S. et al. Exploring Boron applications in modern agriculture: Antifungal activities and mechanisms of Phenylboronic acid derivatives. *Pest Manag. Sci.* **79**, 2748–2761 (2023).
123. Ghelich, R., Jahannama, M. R., Abdizadeh, H., Torknik, F. S. & Vaezi, M. R. Effects of hafnium and Boron on antibacterial and mechanical properties of polyvinylpyrrolidone-based nanofibrous composites. *Polym. Bull.* **79**, 5885–5899 (2022).
124. Lepry, W. C. & Nazhat, S. N. Highly bioactive sol-gel-derived Borate glasses. *Chem. Mater.* **27**, 4821–4831 (2015).
125. Naseri, S., Lepry, W. C., Maisuria, V. B., Tufenkji, N. & Nazhat, S. N. Development and characterization of silver-doped sol-gel-derived Borate glasses with anti-bacterial activity. *J. Non-Cryst. Solids.* **505**, 438–446 (2019).
126. Stoor, P., Söderling, E. & Salonen, J. I. Antibacterial effects of a bioactive glass paste on oral microorganisms. *Acta Odontol. Scand.* **56**, 161–165 (1998).
127. Fernandes, J. S., Gentile, P., Pires, R. A., Reis, R. L. & Hatton, P. V. Multifunctional bioactive glass and glass-ceramic biomaterials with antibacterial properties for repair and regeneration of bone tissue. *Acta Biomater.* **59**, 2–11 (2017).
128. Sornsanit, K., Pudwat, S., Limsuwan, P. & Kaewkha, J. Investigation of antibacterial properties of soda calcium borosilicate glass doped with TiO_2 . *Adv. Mater. Res.* **506**, 525–528 (2012).
129. Yuzheng, W., Xiangxin, X., U. E. & He, Y. Synthesis and antimicrobial activity of boron-doped Titania nano-materials. *Chin. J. Chem. Eng.* **22**, 474–479 (2014).
130. Bachvarova-Nedelcheva, A. et al. Effect of B_2O_3 on the structure, properties and antibacterial abilities of Sol-Gel-Derived $\text{TiO}_2/\text{TeO}_2/\text{B}_2\text{O}_3$ powders. *Materials* **16**, 6400 (2023).
131. Nishikawa, H., Ihara, T., Kasuya, N., Kobayashi, Y. & Takahashi, S. Thermally-induced activation of titanium dioxide and its application to the oxidation of gaseous toluene. *Appl. Surf. Sci.* **479**, 1105–1109 (2019).
132. Lam, P. L. et al. The role of reactive oxygen species in the biological activity of antimicrobial agents: An updated mini review. *Chem.-Biol. Interact.* **320**, 109023 (2020).
133. Mahdy, E. A., Sahbal, K. M., Mabrouk, M., Beherei, H. H. & Abdel-Monem, Y. K. Enhancement of glass-ceramic performance by TiO_2 doping: In vitro cell viability, proliferation, and differentiation. *Ceram. Int.* **47**, 6251–6261 (2021).

Author contributions

All authors of this work sharing each other as a team group, where all of them did his best effort to manage this work.

Funding

Open access funding provided by The Science, Technology & Innovation Funding Authority (STDF) in cooperation with The Egyptian Knowledge Bank (EKB).

Declarations

Competing interests

The authors declare no competing interests.

Ethics approval and consent of participate

The authors of this work agree to send this paper for publication at your interesting journal.

Additional information

Correspondence and requests for materials should be addressed to G.Y.A.-R.

Reprints and permissions information is available at www.nature.com/reprints.

Publisher's note Springer Nature remains neutral with regard to jurisdictional claims in published maps and institutional affiliations.

Open Access This article is licensed under a Creative Commons Attribution 4.0 International License, which permits use, sharing, adaptation, distribution and reproduction in any medium or format, as long as you give appropriate credit to the original author(s) and the source, provide a link to the Creative Commons licence, and indicate if changes were made. The images or other third party material in this article are included in the article's Creative Commons licence, unless indicated otherwise in a credit line to the material. If material is not included in the article's Creative Commons licence and your intended use is not permitted by statutory regulation or exceeds the permitted use, you will need to obtain permission directly from the copyright holder. To view a copy of this licence, visit <http://creativecommons.org/licenses/by/4.0/>.

© The Author(s) 2025